PHYSICAL REVIEW B **93**, 035126 (2016)

Ground-state phase diagram of the square lattice Hubbard model from density matrix embedding theory

Bo-Xiao Zheng and Garnet Kin-Lic Chan[*]
Department of Chemistry, Princeton University, New Jersey 08544, USA

(Received 8 April 2015; revised manuscript received 22 December 2015; published 21 January 2016)

We compute the ground-state phase diagram of the Hubbard and frustrated Hubbard models on the square lattice with density matrix embedding theory using clusters of up to 16 sites. We provide an error model to estimate the reliability of the computations and complexity of the physics at different points in the diagram. We find superconductivity in the ground state as well as competition between inhomogeneous charge, spin, and pairing states at low doping. The estimated errors in the study are below T_c in the cuprates and on the scale of contributions in real materials that are neglected in the Hubbard model.

DOI: 10.1103/PhysRevB.93.035126

The Hubbard model [1–3] is one of the simplest quantum lattice models of correlated electron materials. Its one-band realization on the square lattice plays a central role in understanding the essential physics of high-temperature superconductivity [4,5]. Rigorous, near-exact results are available in certain limits [6]: at high temperatures from series expansions [7–10], in infinite dimensions from converged dynamical mean-field theory [11–14], and at weak coupling from perturbation theory [15] and renormalization group analysis [16,17]. Further, at half filling, the model has no fermion sign problem, and unbiased determinantal quantum Monte Carlo simulations can be converged [18]. Away from these limits, however, approximations are necessary. Many numerical methods have been applied to the model at both finite and zero temperatures, including fixed-node, constrained path, determinantal, and variational quantum Monte Carlo (QMC) [19–29], density matrix renormalization group (DMRG) [30–32], dynamical cluster (DCA) [33,34], (cluster) dynamical mean-field theories (CDMFT) [35,36], and variational cluster approximations (VCA) [37,38]. (We refer to DCA/CDMFT/VCA collectively as Green's function cluster theories.) These pioneering works have suggested rich phenomenology in the phase diagram including metallic, antiferromagnetic, and d-wave (and other kinds of) superconducting phases, a pseudogap regime, inhomogeneous orders such as stripes, and charge, spin, and pair-density waves, as well as phase separation [6,19,20,24,25,27–29,32,35,39–58]. However, as different numerical methods have yielded different pictures of the ground-state phase diagram, a precise quantitative picture of the ground-state phase diagram has yet to emerge.

It is the goal of this paper to produce such a quantitative picture as best as possible across the *full* Hubbard model phase diagram below $U = 8$. Our method of choice is density matrix embedding theory (DMET), which is very accurate in this regime [59–66], employed together with clusters of up to 16 sites and thermodynamic extrapolation. We carefully calibrate errors in our calculations, giving error bars to quantify the remaining uncertainty in our phase diagram. These error bars also serve, by proxy, to illustrate the relative complexity of the underlying physics for different Hubbard parameters. The accuracy we achieve is significantly higher than that attained by earlier comparable Green's function cluster calculations for the ground state. We also carefully estimate the finite size effects, which we find to have a crucial impact on the location of the phase boundaries of the antiferromagnetic and d-wave superconducting (SC) orders, in contrast to some early ground-state studies [41].

The one-band (frustrated) Hubbard model on the $L \times L$ square lattice is

$$H = -t \sum_{\langle ij\rangle\sigma} a^\dagger_{i\sigma} a_{j\sigma} - t' \sum_{\langle\langle ij\rangle\rangle\sigma} a^\dagger_{i\sigma} a_{j\sigma} + U \sum_i n_{i\uparrow} n_{i\downarrow}, \quad (1)$$

where $\langle \cdots \rangle$ and $\langle\langle \cdots \rangle\rangle$ denote nearest and next-nearest neighbors, respectively, $a^{(\dagger)}_{i\sigma}$ destroys (creates) a particle on site i with spin σ, and $n_{i\sigma} = a^\dagger_{i\sigma} a_{i\sigma}$ is the number operator. We study the standard Hubbard model with $t' = 0$ (with $t = 1$) and frustrated models with $t' = \pm 0.2$.

DMET is a cluster impurity method which is exact for weak coupling ($U = 0$) and weak hybridization ($t = 0$) and becomes exact for arbitrary U as the cluster size N_c increases. It differs from Green's function impurity methods such as the DCA or (C)DMFT, as it is a wave-function method, with a *finite* bath constructed to reproduce the entanglement of the cluster with the remaining lattice sites. DMET has recently been applied and benchmarked in a variety of settings from lattice models [59,61–63] to *ab initio* quantum chemistry calculations [64,65] and for ground-state and spectral quantities [66]. In its ground-state formulation, the use of wave functions substantially lowers the cost relative to Green's function impurity methods, allowing larger clusters to become computationally affordable.

We briefly summarize the method here, with details in Appendix A and Refs. [59,60]. DMET maps the problem of solving for the bulk ground state $|\Psi\rangle$ to solving for the ground state of an impurity model with $2N_c$ sites consisting of impurity (physical) and bath (auxiliary) sites. The mapping is defined via the Schmidt decomposition [67] of bulk ground state $|\Psi\rangle$ and is exact as long as $|\Psi\rangle$ is exact. In practice, however, the exact $|\Psi\rangle$ is, of course, unknown. DMET therefore solves an approximate impurity problem defined from a noninteracting *model* bulk wave function $|\Phi\rangle$, the ground state of a quadratic Hamiltonian $h = h_0 + u$, where h_0 is hopping part of the Hubbard Hamiltonian and u is a one-body operator to be determined. Via $|\Phi\rangle$ we define an impurity model Hamiltonian and ground-state $|\Psi'\rangle$ (now an approximation to the exact $|\Psi\rangle$) and from which energies and local observables are measured.

---

[*] gkchan@princeton.edu

The one-body operator u (analogous to the impurity self-energy in DMFT) is determined self-consistently by matching the one-body density matrix of the impurity wave function $|\Psi'(u)\rangle$ and the lattice wave function $|\Phi(u)\rangle$ projected to the impurity model subspace. In this work, we modified the original DMET procedure slightly. First, we allowed u to vary over pairing terms, thus allowing $|\Psi(u)\rangle$ to be a BCS state. Second, we introduced a self-consistent chemical potential to ensure that the filling factors for $|\Phi\rangle$ and $|\Psi'\rangle$ exactly match.

To obtain the ground-state phase diagram, we carried out DMET calculations using 2×2, 4×2, 8×2, and 4×4 impurity clusters, cut from a bulk square lattice with $L = 72$. We considered $t' = 0, \pm 0.2$, $U = 2,4,6,8$, and various densities between $n = 0.6$ and $n = 1$. The impurity model ground state $|\Psi'\rangle$ was determined using a DMRG solver [68] with a maximum number of renormalized states $M = 2000$, allowing for $U(1)$ and $SU(2)$ spin symmetry breaking. The energy, local moment $m = \frac{1}{2}(n_{i\uparrow} - n_{i\downarrow})$, double occupancy $D = \langle n_{i\uparrow} n_{i\downarrow}\rangle$, and local d-wave pairing $d_{sc} = \frac{1}{\sqrt{2}}(\langle a_{i\uparrow} a_{j\downarrow}\rangle + \langle a_{j\uparrow} a_{i\downarrow}\rangle)$ were measured from $|\Psi'\rangle$.

The finite cluster DMET energies and measurements contain three sources of error relative to the exact thermodynamic limit. These are from (i) DMET self-consistency; (ii) finite M in the DMRG solver (only significant for the 16-site impurity clusters), which also induces error in the correlation potential u; (iii) finite *impurity cluster* size. (The error from the use of a finite $L = 72$ bulk lattice is so small as to not affect any of the significant digits presented here.) To estimate the thermodynamic result, we (i) estimated DMET self-consistency error by the convergence of expectation values in the last iterations, (ii) extrapolated DMRG energies and observables with the DMRG density matrix truncation error [69], (iii) estimated the error in u due to finite M, by analyzing expectation values from self-consistent $u(M)$ obtained with different M, (iv) extrapolated cluster size to infinite size, with the $N_c^{-1/2}$ scaling [70] appropriate to a non-translationally-invariant impurity. Each of (i) to (iv) gives an estimate of an uncertainty component (1σ for linear extrapolations), which we combined to obtain a single error bar on the DMET thermodynamic estimates. Details of the error estimation and a discussion of the complete data (of which only a fraction is presented here) are given in SI.

We first verify the accuracy of our thermodynamic estimates and error bars by comparing to benchmark data available at half filling. The data in Table I and Fig. 1(a) show the high accuracy of the DMET energies at half filling. The error bars from DMET, auxiliary-field quantum Monte Carlo [AFQMC, and its constrained path (CP) variant], and DMRG are all consistent with an accuracy better than $0.001t$. Indeed, the DMET error bars are competitive with the exact "statistical" error bars of AFQMC up to $U = 6$. As a point of reference, the DMET uncertainty is one to two orders of magnitude smaller than finite-temperature contributions to recent low-temperature benchmark DCA calculations [Fig. 1(a)] and is similarly two to three orders of magnitude smaller than energy errors in earlier zero-temperature Green's function cluster calculations [75].

Figure 1(c) further gives the half-filling staggered magnetization and double occupancies computed with DMET as compared with AFQMC. The DMET double occupancies are obtained with similar error bars to the AFQMC estimates. The staggered magnetization exhibits larger errors at the smallest $U = 2$ (a cluster size effect) but for $U > 4$ appears similarly, or in fact more accurate than the AFQMC result. At the largest value $U = 12$, we find $m = 0.327(15)$, slightly above the exact Heisenberg value $m = 0.3070(3)$ [76].

TABLE I. Energy of the Hubbard model from various methods. All numbers are extrapolated to the thermodynamic limit. (CP-)AFQMC results are from Qin and Zhang [71]. Note that the half-filling results are numerically exact [72]. DMRG results are from White [73].

U/t	Filling	DMET	AFQMC	CP-AFQMC	DMRG
2	1.0	−1.1764(3)	−1.1763(2)		−1.176(2)
4	1.0	−0.8604(3)	−0.8603(2)		−0.862(2)
6	1.0	−0.6561(5)	−0.6568(3)		−0.658(1)
8	1.0	−0.5234(10)	−0.5247(2)		−0.5248(2)
12	1.0	−0.3686(10)	−0.3693(2)		−0.3696(3)
4	0.8	−1.108(2)		−1.110(3)	−1.1040(14)
4	0.6	−1.1846(5)		−1.185(1)	
4	0.3	−0.8800(3)		−0.879(1)	

The half-filling benchmarks lend confidence to the DMET thermodynamic estimates of the energy and observables and their associated error bars. We therefore use the same error model away from half filling, in the absence of benchmark data. We can verify our error model by comparing to constrained path (CP) AFQMC, a sign-free QMC with a bias that disappears at low density and moderate U [23,24]. For $U = 4$ and $n \leqslant 0.6$, a parameter regime where CP-AFQMC is very accurate, the DMET and CP-AFQMC energies agree to $0.001t$ (Table I). Figure 1(b) shows the energy uncertainties across the phase diagram for $t' = 0$ (The same figure for $t' = \pm 0.2$ is given in SI). As expected, the accuracy away from half filling is significantly lower than at half filling, with the largest errors

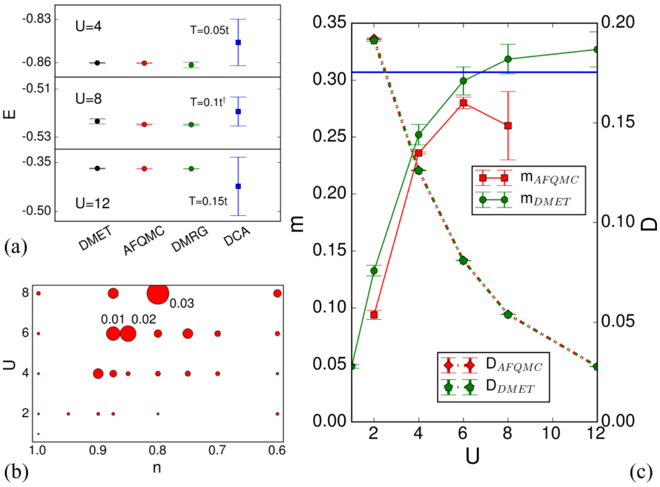

FIG. 1. Benchmark for $t' = 0$ Hubbard model. (a) Ground-state DMET, AFQMC [71], DMRG [73], and low-temperature DCA [74] energies at half filling. †DCA data at $U = 8$ is from a 50-site finite cluster calculation. (b) DMET energy uncertainties. The areas of the circles are proportional to the estimated uncertainties. (c) Staggered magnetization (m) and double occupancy (D) at half filling.

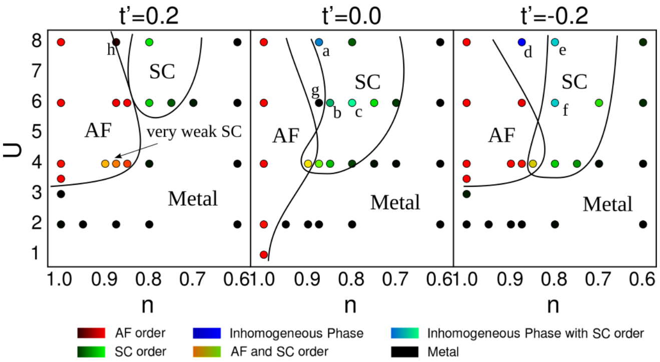

FIG. 2. Phase diagrams of the Hubbard model. Orders are represented with three primary colors: red (antiferromagnetism), green (d-wave superconductivity), and blue (inhomogeneity), with the brightness proportional to the robustness of the order. The points highlighted with letters: (a) local phase separation; (b) d-wave SC with a slight modulation in the (π,π) direction; (c) SC with a weak spin density wave (SDW); (d) a "classic" stripe phase; (e) stripe with pair-density wave (PDW) coexisting with SC; (f) CDW and spin π-phase shift; (g),(h) intermediate points between AF and SC where both order parameters extrapolate to zero. Phase boundaries are guides only.

found in the underdoped region of $n = 0.8$–0.9. The main source of error is from cluster size extrapolation, especially in the underdoped region, where the solution is sensitive to cluster shapes because of phase boundaries and/or the onset of competing inhomogeneous orders.

We present the DMET phase diagrams in Fig. 2. Interestingly, they feature many behaviours previously proposed in different studies. In particular, we observe (i) an antiferromagnetic (AF) phase at half filling; (ii) a metallic phase at large dopings and at small U, enhanced by frustration; (iii) a region of d-wave SC order at intermediate dopings and sufficiently large U; (iv) a region of coexisting AF and SC order; (v) a region rich with inhomogeneous charge, spin, and superconducting orders that are very sensitive to the Hubbard parameters; (vi) points in between the AF and SC phase where the AF and SC orders extrapolate to zero. (The metallic phase is predicted to be unstable at weak coupling and large dopings from weak coupling expansions [17,77], but the relevant parameter region is outside the scope of this paper). At $t' = 0$, for $U = 8$, $n = 0.875$, a SC state with strong inhomogeneity appears which creates large uncertainties in the extrapolated order parameters; thus, the precise location of the SC phase boundary at $U = 8$ is uncertain.

Figure 3 shows the average AF and d-wave SC order parameters as a function of filling for $U = 4$. We find that for $t' = 0$, the peak in SC order is around $\langle n\rangle = 0.9$ and SC extends to $\langle n\rangle \sim 0.8$. The figures also show that next-nearest-neighbor hopping $t' = 0.2$ stabilizes AF versus SC, and the reverse is true for $t' = -0.2$. The suppression (enhancement) of SC order with positive (negative) t' is consistent with the stronger superconductivity found in hole-doped materials [78–80].

The presence of SC in Hubbard model ground state has previously been much discussed. The strongest SC order found in DMET roughly occurs in the same region as seen in earlier Green's function cluster calculations [41,47]. However, this region is not typically found to be superconducting in ground-state wave-function calculations using DMRG and AFQMC on finite lattices, even though such calculations achieve significantly higher energy accuracies than the Green's function cluster studies [25,32,81,82]. The significance of the DMET result is that the energy error bar in this region (e.g., $0.001t$ for $U = 4$, $n = 0.8$, $t' = -0.2$) is comparable to or better than the accurate ground-state wave-function calculations, yet SC order is still seen. This strongly suggests that SC is, in fact, the ground-state order.

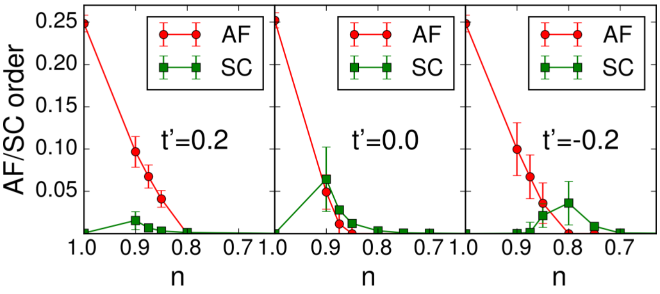

FIG. 3. Antiferromagnetic (red circle) and (d-wave) superconducting (green square) order parameters at $U = 4$.

We now further discuss the intermediate region between the AF and the SC phases. In this region, a variety of spin-density [25,43,45,46,49,83–85], charge-density [25,86–88], pair-density wave [88–91], and stripe orders [30,32,51,52,85,92–95] have been posited in both the Hubbard model and the simpler t-J model, with different types of orders seen in different simulation methods. These inhomogeneous phases are proposed to be relevant in the pseudogap physics [89,90,96–100]. Recent projected entangled pair state (PEPS) studies of the t-J model and Hubbard model at large $U \geqslant 8$ suggest that inhomogeneous and homogeneous states are near degenerate at low doping and can be stabilized with small changes in the model parameters [95,101]. Our work indicates that the Hubbard model behaves similarly. Although we show here in Figs. 4 and 5 only the 8×2 clusters, it is important to note that the 8×2 cluster geometry does not always lead to inhomogeneity, nor are all the 4×4 clusters homogeneous. Instead, at points where the tendency towards inhomogeneity is strong, we find a significant lowering of the energy associated with the inhomogeneous order, reflected either in a much lower energy of an inhomogeneous 8×2 cluster relative to the 4×4 cluster (Fig. 5) or in an inhomogeneity in *both* 8×2 and 4×4 clusters. Thus, while it is not possible with our cluster sizes to extrapolate details of the inhomogeneities in the thermodynamic limit (for example, the particular wavelengths of the spin, charge, and pairing instabilities, or diagonal versus vertical stripe patterns), the evidence points strongly to some forms of inhomogeneity surviving in the thermodynamic limit at the indicated parts of the phase diagram. Interestingly, the kinds of inhomogeneity we observe are extremely rich, and some representative examples are shown in Fig. 4. These correspond to (i) a local phase separation between a half-filled, antiferromagnetic phase and a superconducting ribbon [Fig. 4(a)], (ii) a classic stripe phase order [Fig. 4(b)] very similar to that seen in earlier DMRG ladder studies [32] (there

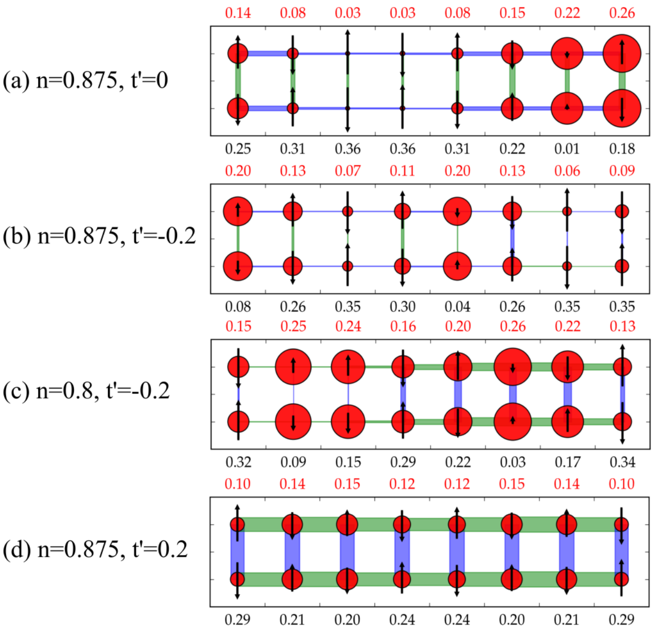

FIG. 4. Local order parameters in the (frustrated) Hubbard model at selected points at $U = 8$.

is also a coexisting weak PDW (exhibiting a sign change across the cell), consistent with earlier stripe proposals [91]), (iii) inhomogeneities in the pairing order coexisting with the charge and spin orders in, e.g., Fig. 4(c), similar to a recent theoretical proposal (see, e.g., Ref. [90]). The inhomogeneity is mainly observed with $t' \leqslant 0$, corresponding to the hole-doped cuprates. Figure 4(d) shows an example at 1/8 doping with positive t', where the inhomogeneity is much weaker.

To summarize, we have computed a ground-state phase diagram for the Hubbard model on the square lattice using cluster DMET. The accuracy achieved by DMET appears competitive with the exact ground-state benchmarks available at half filling, while away from half filling our error model suggests that the calculations remain very accurate. We observe AF and metallic phases and robust d-wave pairing. Further, in parts of the phase space our calculations strongly suggest that inhomogeneous phases are a feature of the thermodynamic limit, although the precise inhomogeneous patterns require larger clusters to resolve and reflect competition between different orders at very low energy scales. However, for real materials such as the cuprates ($t \approx 3000$ K), the energy resolution achieved here for most of the phase diagram is already below the superconducting T_c, suggesting that the near degeneracy of competing orders will be lifted by terms beyond those in the Hubbard model, such as long-range charge and hopping terms, multiorbital effects, and interlayer coupling. Moving beyond the Hubbard model to more realistic material models thus now appears of principal relevance.

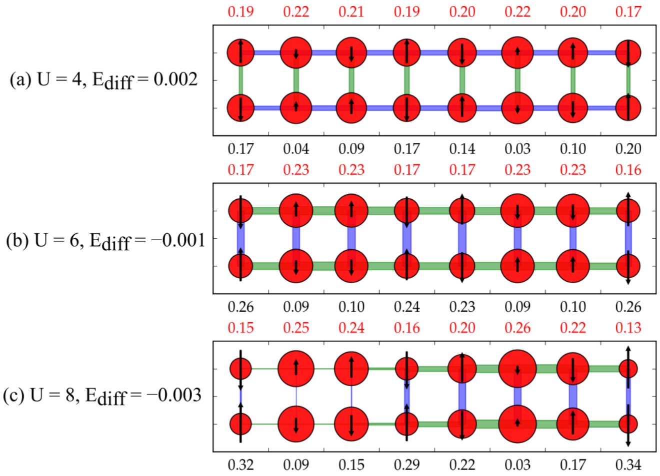

FIG. 5. Evolution of inhomogeneous patterns and stabilities for $n = 0.8$, $t' = -0.2$ at various coupling strengths. $E_{\rm diff}$ is the energy difference between 8×2 and 4×4 impurity cluster calculations. At $U = 8$, both 16-site cluster solutions are inhomogeneous.

ACKNOWLEDGMENTS

We acknowledge funding from the US Department of Energy, Office of Science, through Grants No. DE-SC0008624 and No. DE-SC0010530. This work was also performed as part of the Simons Collaboration on the Many Electron Problem, sponsored by the Simons Foundation. We thank Steven White and Shiwei Zhang for providing unpublished data and Emanuel Gull for helpful comments. We also thank Sandeep Sharma for discussion on implementing DMRG with broken particle number symmetry. Further discussion of the methodology and results can be found in Appendices.

APPENDIX A: SUMMARY OF DMET

Figure 6 illustrates the computational flow of a DMET calculation. A DMET self-consistency cycle consists of (i) solving for the ground state of the DMET lattice Hamiltonian, (ii) building the impurity Hamiltonian, (iii) solving for the impurity Hamiltonian ground-state and observables, and (iv) fitting the DMET correlation potential. As discussed in the main text, in this work we allow the DMET solutions to spontaneously break particle number and spin symmetry. We also include a chemical potential in the self-consistency. Here we explain some general aspects of practical DMET calculations which have not been discussed in detail in the existing literature, as well as describe the technical extensions

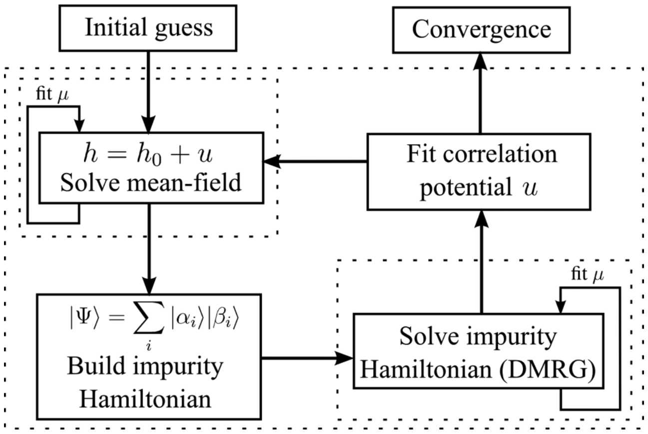

FIG. 6. Graphical representation of the DMET procedure.

to broken particle number symmetry, and the self-consistency procedure for the additional chemical potential.

1. DMET correlation potential

A general DMET correlation potential is a quadratic operator. It is local in the sense that it does not have cross terms between different images of the impurity cluster on the lattice. In the original DMET paper [59], it took the form

$$u = \sum_C u_C = \sum_C \sum_{i,j \in C,\sigma} v_{ij\sigma} a^\dagger_{i\sigma} a_{j\sigma}. \tag{A1}$$

In Eq. (A1), C ranges over all impurity cluster supercells within the (large) lattice, i,j range over sites in the same cluster C, and $\sigma \in \{\alpha,\beta\}$ denotes the two flavors of spin. In this form, the correlation potential has $N_c(N_c+1)/2$ free parameters (here and later on, we assume real potentials), where N_c is the number of sites in the impurity cluster. For spontaneously broken particle number and spin symmetry, the correlation potential acquires additional terms,

$$u = \sum_C \sum_{i,j\in C,\sigma} v_{ij,\sigma} a^\dagger_{i\sigma} a_{j\sigma} + \Delta_{ij} a^\dagger_{i\alpha} a^\dagger_{j\beta} + \text{H.c.} \tag{A2}$$

In this work, we only allow singlet pairing (strictly speaking, $S_z = 0$ pairing) but it is straightforward to extend the above to triplet pairing. The normal part v has two spin components. The pairing term Δ has N_c^2 free parameters (it is symmetric when spin symmetry is preserved, but we allow for spin symmetry breaking). In total, the correlation potential u has $N_c(2N_c+1)$ degrees of freedom.

2. DMET lattice Hamiltonian

The DMET lattice Hamiltonian (including a chemical potential term $-\mu n$) is

$$\begin{aligned} h' &= h + u - \mu n \\ &= \sum_{ij\sigma} h_{ij\sigma} a^\dagger_{i\sigma} a_{j\sigma} + \Delta_{ij} a^\dagger_{i\alpha} a^\dagger_{j\beta} + \text{c.c.}, \end{aligned} \tag{A3}$$

where $h = t + v - \mu$ is the normal one-body term from the hopping, correlation potential, and chemical potential. h' can be rewritten in the form of a spin-unrestricted Bogoliubov-de Gennes (BdG) [102,103] equation,

$$\begin{aligned} \begin{pmatrix} h'_\alpha & \Delta \\ \Delta^T & -h'_\beta \end{pmatrix} \begin{pmatrix} U_\alpha \\ V_\beta \end{pmatrix} &= \begin{pmatrix} U_\alpha \\ V_\beta \end{pmatrix} \varepsilon_\alpha, \\ \begin{pmatrix} h'_\beta & -\Delta^T \\ -\Delta & -h'_\alpha \end{pmatrix} \begin{pmatrix} U_\beta \\ V_\alpha \end{pmatrix} &= \begin{pmatrix} U_\beta \\ V_\alpha \end{pmatrix} \varepsilon_\beta. \end{aligned} \tag{A4}$$

These coupled equations are expressed concisely as

$$\begin{aligned} &\begin{pmatrix} h'_\alpha & \Delta \\ \Delta^T & -h'_\beta \end{pmatrix} \begin{pmatrix} U_\alpha & V_\alpha \\ V_\beta & U_\beta \end{pmatrix} \\ &\quad = \begin{pmatrix} U_\alpha & V_\alpha \\ V_\beta & U_\beta \end{pmatrix} \begin{pmatrix} \varepsilon_\alpha & \\ & -\varepsilon_\beta \end{pmatrix}, \end{aligned} \tag{A5}$$

where ε_α and ε_β are both positive. h' is diagonalized by transforming to the Bogoliubov quasiparticles,

$$c^\dagger_{i\alpha} = u^\alpha_{ji} a^\dagger_{j\alpha} + v^\beta_{ji} a_{j\beta}, \quad c^\dagger_{i\beta} = u^\beta_{ji} a^\dagger_{j\beta} + v^\alpha_{ji} a_{j\alpha}. \tag{A6}$$

Note that the number of $\{c^\dagger_\alpha\}$ and $\{c^\dagger_\beta\}$ quasiparticles will differ if $S_z \neq 0$ in the physical ground state.

In terms of the quasiparticles, the lattice Hamiltonian in Eq. (A3) is diagonalized as

$$h' = E_0 + \sum_{i\sigma} \varepsilon_{i\sigma} c^\dagger_{i\sigma} c_{i\sigma} \tag{A7}$$

and the (ground-state) quasiparticle vacuum $|-\rangle$, defined by $c_{i\sigma}|-\rangle = 0$, has energy E_0. The quasiparticle vacuum is also known as the Bardeen-Cooper-Schrieffer (BCS) ground state [104].

3. DMET impurity model Schmidt subspace

We now discuss how to define the impurity model Schmidt subspace corresponding to a BCS ground state of the lattice Hamiltonian in Eq. (A3). To start, we review the “product space” construction of the impurity model Schmidt subspace, starting from the lattice Hamiltonian Slater determinant ground state, as used in the original DMET [59,60].

The original DMET impurity model consists of a set of impurity sites augmented by a set of bath modes. In Ref. [60], the bath modes are defined through the *projected overlap matrix* of the Slater determinant. We compute the projected overlap matrix from the Slater determinant coefficient matrix,

$$C_0 = \begin{pmatrix} M \\ N \end{pmatrix}_{N\times n}, \tag{A8}$$

where the rows denote physical sites (N sites in total) and columns are occupied modes (orbitals). The upper part M has N_c rows, which correspond to the N_c impurity sites. The projected overlap matrix is

$$S = M^T M. \tag{A9}$$

From the singular value decomposition (SVD) of M as $M = L\Sigma R^T$ (where we use the “full” form of the SVD, L is $N_c \times N_c$, Σ is $N_c \times n$, and R is $n \times n$), then $S = R(\Sigma^T\Sigma)R^T$; i.e., R is the eigenvector matrix of the projected overlap matrix. R defines a unitary transformation of the occupied modes in C_0, giving a new coefficient matrix $C = C_0 R$, where

$$C = \begin{pmatrix} L\Sigma \\ NR \end{pmatrix} = \begin{pmatrix} A & 0 \\ B & D \end{pmatrix} \tag{A10}$$

and the second equality follows because Σ is a rectangular matrix of the form $[\text{diag}(\sigma),\mathbf{0},\mathbf{0},\ldots\mathbf{0}]$, where the first N_c columns constitute a diagonal matrix, and the remaining $n - N_c$ columns are zero columns. The first N_c columns of C, $\binom{A}{B}$, define the *embedding modes*, which have nonzero weight on the impurity sites. The matrix B defines the *bath modes*, which may be orthonormalized using the QR decomposition, $B = QR$. The remaining columns in C define the *core modes*, which have no weight on the impurity. The Schmidt subspace is then $\mathcal{F}(a^\dagger_i) \otimes \mathcal{F}(b^\dagger_i) \otimes |e_1 \cdots e_{n-N_c}\rangle$, where $\{a^\dagger_i\}$ create electrons in the impurity modes, $\{b^\dagger_i\}$ create electrons in the bath modes (from the columns of Q), and $|e_1 \cdots e_{n-N_c}\rangle$ is the core state, defined by the columns of D. The coefficients defining $\{a^\dagger_i\}$, $\{b^\dagger_i\}$ can be gathered in the columns of a matrix C_1,

$$C_1 = \begin{pmatrix} I_{N_c} & \\ & Q \end{pmatrix}, \tag{A11}$$

where I_{N_c} is an $N_c \times N_c$ identity matrix.

A and B can also be obtained directly from the one-particle density matrix. The rotation between C and C_0 leaves the one-body density matrix invariant; thus,

$$\rho = \langle a_i^\dagger a_j\rangle = C_0 C_0^T = CC^T$$
$$= \begin{pmatrix} AA^T & AB^T \\ BA^T & BB^T + DD^T \end{pmatrix} \equiv \begin{pmatrix} \rho_{\text{imp}} & \rho_c^T \\ \rho_c & \rho_{\text{env}} \end{pmatrix}. \quad \text{(A12)}$$

Defining the eigendecomposition $\rho_{\text{imp}} = U\Lambda U^T$, we find

$$A = U\Lambda^{\frac{1}{2}} \text{ and } B = \rho_c (A^T)^{-1}. \quad \text{(A13)}$$

The above defines the impurity model Schmidt subspace as a tensor product of the impurity site space and a bath space; thus, we refer to it as a "product-space" embedding construction. However, for the BCS state, it is easier to use a slightly different, but equivalent construction. We explain this first for the Slater determinant. Here we build an $L \times 2N_c$ matrix C_2, whose columns span the same vector space as C_1 in Eq. (A11), but which does not have the block structure. We start with the "hole" one-particle density matrix,

$$\rho_h = \langle a_i a_j^\dagger\rangle = I - \rho^T = I - \rho. \quad \text{(A14)}$$

We can replace ρ with ρ_h in Eqs. (A12) and (A13) and compute an analogous set of coefficients A' and B'. Taking A, B, and A', B' gives C_2,

$$C_2 = \begin{pmatrix} A & A' \\ B & B' \end{pmatrix}_{N\times 2N_c}. \quad \text{(A15)}$$

The $2N_c$ columns of C_2 span *exactly the same space* as C_1 (proved in the Sec. 7 of this appendix). Thus, we can equivalently define the Schmidt subspace from the columns of C_2, as we can from C_1. Transforming to the quasiparticle vacuum of the Slater determinant, $|-\rangle$, the columns of C_2 define a set of $2N_c$ quasiparticle creation operators,

$$c_{i\sigma}^\dagger = \sum_{j\in\text{imp}} A_{ji} a_{j\sigma'} + \sum_{j\in env} B_{ji} a_{j\sigma'}, \quad \text{(A16)}$$

$$c_{\bar{i}\bar{\sigma}}^\dagger = \sum_{j\in\text{imp}} A'_{j\bar{i}} a_{j\sigma}^\dagger + \sum_{j\in env} B'_{j\bar{i}} a_{j\sigma}^\dagger, \quad \text{(A17)}$$

that yields the Schmidt subspace as $\mathcal{F}(\{\bar{c}_{i(\bar{i})\sigma}^\dagger\}) \otimes |-\rangle$. As the impurity model Schmidt subspace here does not (transparently) separate between the impurity sites and environment sites, but rather involves a set of modes which are a linear transformation of both the occupied and the virtual modes in the Slater determinant, we refer to this as a "quasiparticle embedding" construction. This provides an alternative view of the DMET embedding as an active space method that uses the embedding quasiparticles defined from C_2 as the active space, while freezing other excitations that involve only the environment.

Extending the quasiparticle embedding construction to BCS states is straightforward. By analogy with the one-particle density matrix of a Slater determinant, we define the generalized one-body density matrix for BCS states,

$$G_\sigma = \begin{pmatrix} U_\sigma \\ V_{\bar{\sigma}} \end{pmatrix} \begin{pmatrix} U_\sigma^T & V_{\bar{\sigma}}^T \end{pmatrix} = \begin{pmatrix} 1-\rho_\sigma & \kappa_\sigma \\ \kappa_\sigma^T & \rho_{\bar{\sigma}} \end{pmatrix}, \quad \text{(A18)}$$

where the normal one-particle density matrices $\rho_\sigma = \langle a_{i\sigma}^\dagger a_{j\sigma}\rangle = V_\sigma V_\sigma^T = 1 - U_\sigma U_\sigma^T$ and the pairing density matrix $\kappa = \langle a_{i\alpha} a_{j\beta}\rangle = \kappa_\alpha = -\kappa_\beta^T = U_\alpha V_\beta^T$. The diagonal of G is formed by the hole and particle density matrices, and the off-diagonals are formed by the pairing matrix. When the BCS state degenerates to a Slater determinant, $\kappa = 0$.

We reorganize the generalized density matrix G into impurity and environment blocks, placing the impurity (environment) submatrices of ρ and κ together,

$$G = \begin{pmatrix} G_{\text{imp}} & G_c^T \\ G_c & G_{\text{env}} \end{pmatrix}. \quad \text{(A19)}$$

For instance, the impurity block is

$$G_{\text{imp}} = \begin{pmatrix} 1-\rho_\sigma^{\text{imp}} & \kappa_\sigma^{\text{imp}} \\ \left(\kappa_\sigma^{\text{imp}}\right)^T & \rho_{\bar{\sigma}}^{\text{imp}} \end{pmatrix}_{2N_c\times 2N_c}. \quad \text{(A20)}$$

Then, similar to the treatment in Eq. (A13), we rewrite the impurity part of the generalized density matrix $G_{\text{imp}} = \bar{A}\bar{A}^T$ and define a rotated quasiparticle coefficient matrix,

$$C_2 = \begin{pmatrix} \bar{U}_{\sigma,\text{imp}} \\ \bar{V}_{\bar{\sigma},\text{imp}} \\ \bar{U}_{\sigma,\text{env}} \\ \bar{V}_{\bar{\sigma},\text{env}} \end{pmatrix} = \begin{pmatrix} G_{\text{imp}} \\ G_c \end{pmatrix} (\bar{A}^T)^{-1} = \begin{pmatrix} \bar{A} \\ \bar{B} \end{pmatrix}_{2N\times 2N_c}, \quad \text{(A21)}$$

where $\bar{B} = G_c(\bar{A}^T)^{-1}$. Equation (A21) defines a new set of quasiparticles (with associated quasiparticle creation operators $\{\bar{c}_{i\sigma}^\dagger\}$) in Eq. (A6) through the coefficients $\bar{U}_\sigma, \bar{V}_\sigma$. These are a unitary rotation of the original $2L$ quasiparticles such that only $2N_c$ of them have nonzero overlap with the impurity. As the rotation does not mix the quasiparticle creation and annihilation operators, the vacuum of $\bar{c}_{i\sigma}$ is still the BCS ground state $|-\rangle$. In analogy to the embedding for Slater determinants, the Schmidt subspace is now spanned by the embedding quasiparticles, $\mathcal{F}(\{\bar{c}_{i\sigma}^\dagger\}) \otimes |-\rangle$.

To connect with Eq. (A15), note that when the BCS state is a Slater determinant, G_{imp} and G_c are both block diagonal, and, thus, $\bar{A} = \text{diag}(A'^\sigma, A^{\bar{\sigma}})$, $\bar{B} = \text{diag}(B'^\sigma, B^{\bar{\sigma}})$, and Eq. (A21) becomes

$$\bar{U}_\sigma = \begin{pmatrix} A'^\sigma & 0 \\ B'^\sigma & 0 \end{pmatrix}, \quad \text{(A22)}$$

$$\bar{V}_{\bar{\sigma}} = \begin{pmatrix} 0 & A^{\bar{\sigma}} \\ 0 & B^{\bar{\sigma}} \end{pmatrix}. \quad \text{(A23)}$$

Combining both sets of spins, the quasiparticles in Eq. (A23) then span exactly the same Hilbert space as the basis defined in Eq. (A15). For general BCS ground states, however, $\bar{A}$ and $\bar{B}$ are not block diagonal, and the embedding quasiparticles are mixtures of particles and holes.

The above gives the quasiparticle embedding construction for the BCS state. In the case of the Slater determinant, we started with the equivalent product space embedding, the relation between the two being given by the unitary transformation between the matrix C_2 and C_1, which has block diagonal form. In the case of the C_2 matrix in Eq. (A21), there does not exist a *unitary* transformation that separates the quasiparticles into N_c impurity modes and N_c bath modes.

One can, however, use a *Bogoliubov* transformation to separate the impurity and bath degrees of freedom, accompanied by a renormalization of the vacuum. This then gives rise to a "product space" embedding for the BCS state.

To show this, we only need to write the BCS state as a product state, as described in Ref. [105]. We define a simple vacuum $|\mathrm{vac}\rangle$ as a ferromagnetic state where all L physical sites are occupied with a spin-down (β) electron, and let

$$d_{i\alpha}^{\dagger} = c_{i\beta}, \tag{A24}$$

where the $\{c_{i\sigma}\}$ are the quasiparticle creation operators defined in Eq. (A6). $\{d_{i\alpha}^{\dagger}\}$ are correspondingly quasiparticles for the ferromagnetic vacuum $|\mathrm{vac}\rangle$, since $d_{i\alpha}\,|\mathrm{vac}\rangle = 0$ since $|\mathrm{vac}\rangle$ is already the lowest eigenstate of S_z.

The BCS ground state $|-\rangle$ is the quasiparticle vacuum of $\{c_{i\sigma}\}$. This means that it can be written as (up to a phase)

$$|-\rangle = \prod_i d_{i\alpha}^{\dagger}|\mathrm{vac}\rangle, \tag{A25}$$

since $c_{i\sigma} d_{i\sigma}^{\dagger} = 0$. Equation (A25) rewrites the BCS state into a product state representation (the vacuum $|\mathrm{vac}\rangle$ is also a product state). We can then take the "occupied" modes ($\{d_{i\alpha}\}$) and use the standard product space construction for Slater determinants to write the Schmidt decomposition,

$$|-\rangle = \prod_{i\in N_c}(p_i a_{i\alpha}^{\dagger} + q_i b_{i\alpha}^{\dagger})|\mathrm{vac}\rangle_{\mathrm{imp}} \otimes \prod_{j\in L-N_c} \bar{d}_{j\alpha}^{\dagger}|\mathrm{vac}\rangle_{\mathrm{env}}, \tag{A26}$$

where $\{a_{i\alpha}^{\dagger}\}$ and $\{b_{i\alpha}^{\dagger}\}$ are impurity and bath modes, and $\{\bar{d}_{j\alpha}^{\dagger}\}$ are the "core" environment modes. In fact, $b_{i\alpha}^{\dagger}$ is simply the (normalized) environment part of $\bar{c}_{i\beta}$, and the Schmidt space is $\mathcal{F}(\{a_{i\alpha}^{\dagger}\}) \otimes \mathcal{F}(\{b_{i\alpha}^{\dagger}\}) \otimes \prod_{j\in L-N_c} \bar{d}_{j\alpha}^{\dagger}|\mathrm{vac}\rangle_{\mathrm{env}}$. Since the core wave function now becomes $\prod_{j\in L-N_c} \bar{d}_{j\alpha}^{\dagger}|\mathrm{vac}\rangle_{\mathrm{env}}$ instead of the BCS ground state $|-\rangle$, one has to explicitly include the contributions of the core state in observables.

The quasiparticle embedding and the product state embedding are equivalent theoretically, and in this work we use the quasiparticle approach. However, the resulting embedding modes are delocalized, which increases the entanglement of the impurity model which needs to be captured in the DMRG solver. Thus, for larger clusters, we believe the product space approach may prove favorable from a computational point of view.

4. DMET impurity Hamiltonian and DMRG solver

Once the Schmidt subspace has been defined, the DMET Hamiltonian is formally obtained by projecting an interacting lattice Hamiltonian into the subspace as $H_{\mathrm{imp}} = PH'P$, with the many-particle projector defined as

$$P = \sum_{\vec{n}_{i\sigma}} |\Psi_{\vec{n}_{i\sigma}}\rangle\langle\Psi_{\vec{n}_{i\sigma}}|, \tag{A27}$$

where $\vec{n}_{i\sigma}$ is a vector of occupation numbers of the embedding quasiparticles and $|\Psi_{\vec{n}_{i\sigma}}\rangle = \prod_{n_{i\sigma}} (c_{i\sigma}^{\dagger})^{n_{i\sigma}}|-\rangle$. In earlier DMET work, two choices of lattice Hamiltonian were used in the projection: the original interacting lattice Hamiltonian H (in this case the original Hubbard Hamiltonian) and a modified interacting lattice Hamiltonian H', where the interaction term U is only used in the impurity sites. As in earlier DMET work on lattice models, here we use the latter simpler Anderson-like lattice Hamiltonian H'. In H', on the environment sites (outside of the impurity cluster) the Coulomb interaction U is replaced with the correlation potential u, giving

$$H' = h + \sum_{C\neq\mathrm{imp}} u_C + \sum_{i\in\mathrm{imp}} U n_{i\alpha} n_{i\beta} - \mu n. \tag{A28}$$

The projection defined in Eq. (A27) reduces to transforming $\{a_{i\sigma}^{(\dagger)}\}$ to the embedding quasiparticle basis using the inverse Bogoliubov transformation,

$$a_{i\sigma}^{\dagger} = u_{ij}^{\sigma} c_{j\sigma}^{\dagger} + v_{ij}^{\sigma} c_{j\bar{\sigma}}, \tag{A29}$$

and replacing the pure environment quasiparticle operators with their expectation values with the BCS ground state $|-\rangle$.

After projection, we can write H_{imp} as a sum of one- and two-particle parts, $H_{\mathrm{imp}} = h_{\mathrm{imp}} + V_{\mathrm{imp}}$, where h_{imp} is

$$h_{\mathrm{imp}} = \bar{h}_{ij}^{\sigma} c_{i\sigma}^{\dagger} c_{j\sigma} + \bar{\Delta}_{ij} c_{i\alpha}^{\dagger} c_{j\beta}^{\dagger} + \mathrm{c.c.} + E_0 \tag{A30}$$

and $c_{i\sigma}^{(\dagger)}$ here denote the embedding quasiparticles. In terms of the Bogoliubov coefficients of the embedding quasiparticles U_σ, V_σ, the components of h_{imp} are defined as

$$\begin{aligned}
\bar{h}^{\alpha} &= U_\alpha^T h_\alpha U_\alpha - V_\beta^T h_\beta V_\beta + U_\alpha^T \Delta V_\beta + V_\beta^T \Delta^T U_\alpha,\\
\bar{h}^{\beta} &= U_\beta^T h_\beta U_\beta - V_\alpha^T h_\alpha V_\alpha - U_\beta^T \Delta^T V_\alpha - V_\alpha^T \Delta U_\beta,\\
\bar{\Delta} &= U_\alpha^T \Delta U_\beta + V_\beta^T \Delta^T V_\alpha - V_\beta^T h_\beta U_\beta + U_\alpha^T h_\alpha V_\alpha,\\
E_0 &= \mathrm{Tr}\left(V_\beta^T h_\beta V_\beta + V_\alpha^T H_\alpha V_\alpha + V_\alpha^T \Delta U_\beta + U_\beta^T \Delta^T V_\alpha\right),
\end{aligned} \tag{A31}$$

where h_σ and Δ are the one-particle and pairing terms in the lattice Hamiltonian, respectively. The two-particle part V contains many contributions due to the breaking of particle number symmetry in the quasiparticle formulation. These have the form

$$\begin{aligned}
V_{\mathrm{imp}} = {}& \frac{1}{2}\sum_{pqsr,\sigma\mu} w_{pqsr,\sigma\mu} c_{p\sigma}^{\dagger} c_{q\mu}^{\dagger} c_{s\mu} c_{r\sigma}\\
&+ \sum_{pq,\sigma} h_{pq,\sigma} c_{p\sigma}^{\dagger} c_{q\sigma} + E_1\\
&+ \frac{1}{4}\sum_{pqsr} x_{pqsr} c_{p\alpha}^{\dagger} c_{q\alpha}^{\dagger} c_{s\beta}^{\dagger} c_{r\beta}^{\dagger}\\
&+ \frac{1}{2}\sum_{pqsr,\sigma} \tilde{v}_{pqsr,\sigma} c_{p\sigma}^{\dagger} c_{q\sigma}^{\dagger} c_{s\bar{\sigma}}^{\dagger} c_{r\sigma}\\
&+ \sum_{pq} \Delta_{pq} c_{p\alpha}^{\dagger} c_{q\beta}^{\dagger} + \mathrm{c.c.}
\end{aligned} \tag{A32}$$

V_{imp} connects N-particle states with $N, N\pm 2, N\pm 4$ states. For brevity, we do not give the formulas for the coefficients explicitly [which are obtained by simple algebra from Eq. (A29)]. The scalar and one-particle terms in V_{imp} contain contributions from pure environment quasiparticles and can be absorbed into h_{imp}.

We have adapted our quantum chemistry DMRG code BLOCK [106–108] to break $U(1)$ particle number symmetry and to incorporate the Hamiltonian terms in Eqs. (A30) and (A32). While the full wave function is not restricted to $U(1)$

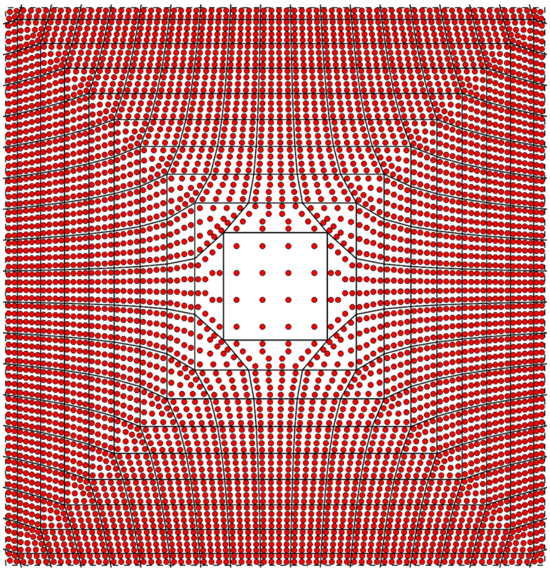

FIG. 7. The effect of the deform function $p(r)$ used in the quasiparticle localization procedure. The figure shows a deformed 72×72 (periodic) lattice with a 4×4 impurity cluster.

symmetry, the particle quantum number is still used in the calculations in the sense that the renormalized states are required to carry a definite particle number. This allows us to use the block sparsity of the Hamiltonian to tackle larger numbers of renormalized states.

The quasiparticle basis associated with $c_{i\sigma}^{(\dagger)}$ is not localized to a site; thus, we use a localization and ordering procedure as used in quantum chemistry DMRG calculations to reduce long-range entanglement between the embedding quasiparticles. We define a center for each quasiparticle and minimize the metric

$$d = \sum_i \langle [p(r_i) - p(r_{i0})]^2 \rangle, \tag{A33}$$

where r_{i0} is the center for $c_{i\sigma}^{(\dagger)}$. The centers are assigned to the impurity sites, with two centers per site. A simple mapping $p(r)$ deforms the lattice (Fig. 7) to prioritize the localization of the sites within and nearby the impurity cluster, which are more entangled because of the interaction. The localized quasiparticles are then reordered according to the position of their centers r_{i0}. We find that the localization and reordering significantly reduce the DMRG truncation error, by up to a factor of 10.

5. Expectation values

As discussed in the original papers on DMET [60], the DMET energy of H_{imp} defined in Eq. (A30) does not correspond to the ground-state energy of the impurity cluster. This is because the impurity Hamiltonian contains three types of energy contributions: pure impurity, impurity-bath interactions, and pure bath (environment) parts. The proper DMET energy should exclude the pure environment contributions and include only part of the impurity-bath interaction energy. Therefore, the DMET energy is evaluated as a *partial* trace of the one- and two-particle reduced density matrices of the impurity wave function. This partial trace can be equivalently implemented as a full trace, with appropriate scaling factors for terms in the Hamiltonian which couple the impurity and environment. For each class of term in the Hamiltonian, this scaling factor is given by the number of indices in the impurity, divided by the total number of indices. (For example, for the one-particle terms in the Hamiltonian, the contribution of the impurity-bath block to the total trace is scaled by a factor of $\frac{1}{2}$.)

An equivalent formulation for the Hubbard Hamiltonian (which contains no long-range Coulomb terms) is to evaluate the two-particle part of DMET energy as

$$E_2 = \langle \Psi | V_{\text{imp}} | \Psi \rangle = E_{\text{DMRG}} - \langle \Psi | h_{\text{imp}} | \Psi \rangle, \tag{A34}$$

where $|\Psi\rangle$ is the DMRG ground state. Since h_{imp} is a quadratic operator, E_2 can be computed only with knowledge of the DMRG energy and the one-particle (and pairing) density matrix, avoiding explicitly evaluating $\langle \Psi | V_{\text{imp}} | \Psi \rangle$ through the two-particle density matrix.

The local spin moments and pairing are both one-particle quantities. We therefore obtain them from the one-particle and pairing density matrix $\rho = \langle c_{i\sigma}^\dagger c_{j\sigma} \rangle$, $\kappa = \langle c_{i\alpha} c_{j\beta} \rangle$ of the DMRG wave function $|\Psi\rangle$, transformed back to the lattice site basis $\{a_{i\sigma}^{(\dagger)}\}$ using Eq. (A29). Note that ρ and κ are defined not only for quasiparticles inside the impurity Schmidt subspace, but also for core quasiparticles. [In the quasiparticle approach, although ρ and κ are themselves zero in the core, terms such as $c_i c_j^\dagger$ can appear in the expansion using Eq. (A29) and result in nonzero expectation values.] If one is interested only in impurity cluster expectation values or DMET lattice Hamiltonians without broken symmetry, the contribution of the core quasiparticles is strictly zero and may thus be omitted. However, for ordered (e.g., magnetic or superconducting) states, the core contribution does not vanish and therefore *cannot* be neglected. Doing so would produce, for example, the strange result of vanishing long-range correlations even in a long-range ordered DMET state.

In this study, when a single value of the order parameter is given, it is computed using the 2×2 plaquette at the center of the impurity cluster, to minimize the boundary effects. The antiferromagnetic order parameter is defined as

$$m = \tfrac{1}{4}(m_{0,0} + m_{1,1} - m_{0,1} - m_{1,0}) \tag{A35}$$

and the d-wave parameter as

$$d = \tfrac{1}{4}[d_{(0,0),(0,1)} + d_{(1,0),(1,1)} - d_{(0,0),(1,0)} - d_{(0,1),(1,1)}], \tag{A36}$$

where $m_i = \frac{1}{2}(n_{i\alpha} - n_{i\beta})$ and $d_{ij} = \frac{1}{\sqrt{2}}(\langle a_{i\alpha} a_{j\beta} \rangle + \langle a_{j\alpha} a_{i\beta} \rangle)$, as defined in the main text. At some points in the phase diagram there are also inhomogeneous states. When the inhomogeneity is strong, we report here the full distribution of local order parameters.

6. DMET self-consistency

The DMET embedding constructs the impurity model via the model ground state of the DMET lattice Hamiltonian; however, this state (and the lattice Hamiltonian) is a function of the correlation potential u. u is determined by the self-consistency procedure, which aims to minimize the difference between the embedding wave function and the DMET mean-field wave function, as measured by their (generalized) one-particle density matrix difference. In the quasiparticle embedding space, the one-particle and pairing density matrices of the mean-field wave function $|\Phi\rangle$ are simply zero. Conceptually, the simplest technique is to define u to minimize the Frobenius norm,

$$\begin{aligned}\min_u \|G_{\Psi(u)} - G_{\Phi(u)}\|_F \\ = \min_u \sum_{ij} \left(\left|\rho^{\alpha}_{\Psi,ij}\right|^2 + \left|\rho^{\beta}_{\Psi,ij}\right|^2 + 2\left|\kappa_{\Psi,ij}\right|^2\right).\end{aligned} \tag{A37}$$

However, as the derivative of the correlated wave function $|\Psi\rangle$ with respect to u is expensive, the above is solved in a two-step procedure consisting of an inner and an outer loop. In the inner loop, we carry out $\min_u \|G_\Psi - G_{\Phi(u)}\|_F$, i.e., the correlated wave function is held fixed, while in the outer loop, the updated u leads to a new impurity model and a new correlated wave function Ψ. Since the correlation potential is restricted to the impurity, while the generalized density matrices range over the whole embedded system (impurity + bath), the Frobenius norm does not vanish and is minimized in the least-squares sense in Eq. (A37). Other choices of self-consistency condition, where the metric vanishes, can also be formulated but are not used here.

If the total particle number n is allowed to fluctuate, as in a superconducting state, then one of the conjugate pairs (chemical potential) μ or (particle density) $\langle n\rangle$ must be fixed. We usually want to express the observables as a function of doping, or occupation; thus, we fix $\langle n\rangle$ and determine the appropriate μ. Since the diagonal elements of the correlation potential and chemical potential appear redundant, how can one determine the chemical potential? Formally, at the DMET mean-field level [Eq. (A3)], there is a gauge freedom between u and μ, namely

$$\mu' = \mu + \phi, \quad u' = u + \phi \sum_{i\sigma} a^\dagger_{i\sigma} a_{i\sigma}; \tag{A38}$$

however, this gauge freedom is lost at the embedding stage [Eq. (A28)], because u is only added to the environment (sites outside of the impurity), while μ affects *every* site in the lattice, including the impurity. This difference allows us to use the two-step self-consistency scheme to determine μ, as shown in Fig. 6. Specifically, we first fit μ at the mean-field stage to ensure $\langle n\rangle$ is correct. Then at the embedding stage we vary μ and u simultaneously, following Eq. (A38). This means that the DMET mean-field solution (and thus definition of the impurity model) stays the same, but the relative energy levels of the impurity change as compared to the bath, which allows us to adjust the filling on the impurity.

Fitting at the embedding stage means we need to solve the correlated impurity problem more than once in a single DMET self-consistency iteration. This increases the computational cost. Our strategy is to allow only one iteration of chemical potential fitting in each DMET iteration, corresponding to at most three DMRG calculations. Because fitting μ is a one-dimensional search, even with this crude approach, we can usually control the relative deviation of $\langle n\rangle$ to less than 10^{-4}.

7. Proofs

Here we prove the equivalence of the Fock spaces spanned by C_1 and C_2 in the construction of the impurity Schmidt subspace, as defined in Sec. A 3 of this appendix. Precisely, we need to prove the following.

(1) C_2 is orthonormal; $C_2^T C_2 = I$. (It is easy to see that C_1 is orthonormal, because Q is a unitary matrix from QR decomposition.)

(2) $C_2 = C_1 V$, which is equivalent to $C_1^T C_2 = V$, where V is unitary.

To prove (1) $C_2^T C_2 = I$, we need the idempotency of density matrices $\rho^2 = \rho$. Considering only the upper left block of ρ, we have

$$\rho^2_{\text{imp}} + \rho_c^T \rho_c = \rho_{\text{imp}}. \tag{A39}$$

From Eqs. (A13) and (A14), we know $A' = U(I-\Lambda)^{\frac{1}{2}}, B' = -\rho_c(A'^T)^{-1}$. Therefore,

$$\begin{aligned}C_2^T C_2 &= \begin{pmatrix} A^T & A^{-1}\rho_c^T \\ A'^T & -(A')^{-1}\rho_c^T \end{pmatrix}\begin{pmatrix} A & A' \\ \rho_c(A^T)^{-1} & -\rho_c(A'^T)^{-1} \end{pmatrix} = \begin{pmatrix} A^T A + A^{-1}\rho_c^T\rho_c(A^T)^{-1} & A^T A' - A^{-1}\rho_c^T\rho_c(A'^T)^{-1} \\ A'^T A - (A')^{-1}\rho_c^T\rho_c(A^T)^{-1} & A'^T A' + (A')^{-1}\rho_c^T\rho_c(A'^T)^{-1} \end{pmatrix} \\ &= \begin{pmatrix} \Lambda + \Lambda^{-\frac{1}{2}}\Lambda(I-\Lambda)\Lambda^{-\frac{1}{2}} & \Lambda^{\frac{1}{2}}(I-\Lambda)^{\frac{1}{2}} - \Lambda^{-\frac{1}{2}}\Lambda(I-\Lambda)(I-\Lambda)^{-\frac{1}{2}} \\ (I-\Lambda)^{\frac{1}{2}}\Lambda^{\frac{1}{2}} - (I-\Lambda)^{-\frac{1}{2}}\Lambda(I-\Lambda)\Lambda^{-\frac{1}{2}} & I - \Lambda + (I-\Lambda)^{-\frac{1}{2}}\Lambda(I-\Lambda)(I-\Lambda)^{-\frac{1}{2}} \end{pmatrix} = I.\end{aligned} \tag{A40}$$

For (2), since

$$V = C_1^T C_2 = \begin{pmatrix} A & A' \\ Q^T\rho_c(A^T)^{-1} & -Q^T\rho_c(A'^T)^{-1} \end{pmatrix}, \tag{A41}$$

we have

$$\begin{aligned}VV^T &= \begin{pmatrix} A & A' \\ Q^T\rho_c(A^T)^{-1} & -Q^T\rho_c(A'^T)^{-1} \end{pmatrix}\begin{pmatrix} A^T & A^{-1}\rho_c^T Q \\ A'^T & -A'^{-1}\rho_c^T Q \end{pmatrix} \\ &= \begin{pmatrix} AA^T + A'A'^T & \rho_c^T Q - \rho_c^T Q \\ Q^T\rho_c - Q^T\rho_c & Q^T\rho_c(AA^T)^{-1}\rho_c^T Q + Q^T\rho_c(A'A'^T)^{-1}\rho_c^T Q \end{pmatrix} = \begin{pmatrix} I & 0 \\ 0 & R[A^{-1} + (I-A)^{-1}]R^T \end{pmatrix}.\end{aligned} \tag{A42}$$

In the bottom-right block,

$$\begin{aligned}A^{-1} + (I-A)^{-1} &= U\Lambda^{-1}U^T + U(I-\Lambda)^{-1}U^T \\ &= U\Lambda^{-1}(I-\Lambda)^{-1}U^T = [A(I-A)]^{-1} = (B^T B)^{-1} = (R^T R)^{-1} = R^{-1}(R^T)^{-1}.\end{aligned} \tag{A43}$$

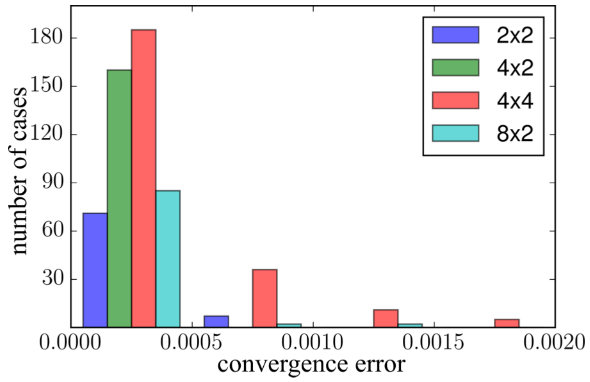

FIG. 8. Distribution and average value (inset) of the DMET self-consistency error in the energy (units of t) for each cluster size.

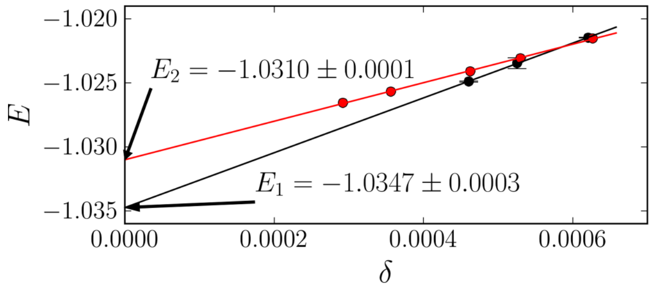

(a)U=4 E = -1.033(2)

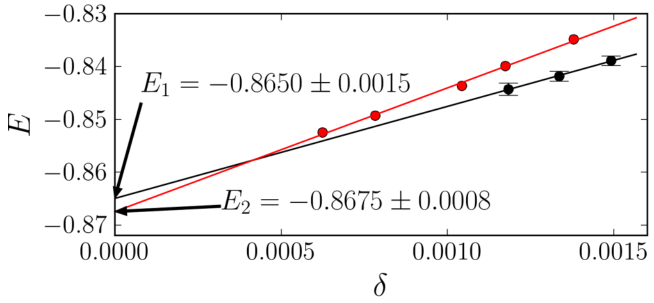

(b)U=6 E = -0.866(2)

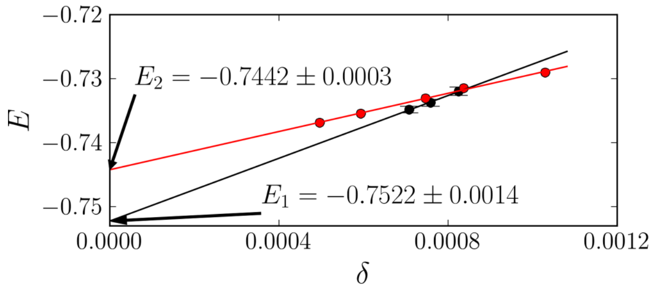

(c)U=8 E = -0.748(4)

FIG. 9. Computations involved in the estimate of the 4×4 cluster DMET energy. The black dots (with error bars for the self-consistency error) are DMET self-consistent results using different DMRG M. These points are extrapolated to obtain E_1. The red dots are DMRG results using the "best" self-consistent correlation potential, which are then extrapolated to obtain E_2. The final 4×4 cluster DMET energies are reported as $E = \frac{1}{2}(E_1 + E_2)$. The plots are shown for $t' = 0, n = 0.875$ and (a) $U = 4$, (b) $U = 6$, (c) $U = 8$.

So $VV^T = I$. Here we assume R is invertible, which is true if and only if we have the full set of N_c bath orbitals coupled to the impurity. This is generally true in lattice settings where the impurity and the environment are strongly coupled. Sometimes the bath can be smaller than the impurity in molecules and when we use a large basis set, and in these cases, special treatment is needed.

APPENDIX B: ERROR MODEL

As described in the main text, we consider three sources of error: (i) errors in DMET self-consistency, (ii) finite M in the DMRG solver, and (iii) finite impurity cluster size. The DMET self-consistency error is estimated as $\frac{1}{2}|E^{(n-1)} - E^{(n)}|$, where $E^{(n)}$ and $E^{(n-1)}$ are the energies of the last two DMET self-consistency iterations. A typical DMET calculation oscillates between two slightly different solutions with the magnitude of the oscillations decreasing with the number of iterations. We use the range of oscillation as a representation of the self-consistency error. The error distributions across the range of calculations in this work are shown in Fig. 8, with the average values in the inset. For most points in the phase diagram, and for all cluster sizes, the self-consistency error is less than $0.0005t$. For 4×4 clusters DMET calculations are the harder to converge, due to larger error in the embedded calculations, giving a largest error of up to $0.002t$ and an average self-consistency error approximately twice as large as that for the other cluster shapes.

For impurity clusters larger than the 2×2 cluster (where our DMRG solver is not exact), there is error due to using finite M in the DMRG impurity solver. The error due to finite M has two components:

(1) variational error in the DMRG calculation, which is usually assumed proportional to the density matrix truncation weight δ_w;

(2) the DMET correlation potential error δ_u, as δ_u is a function of the impurity density matrices, and these have an error for finite M.

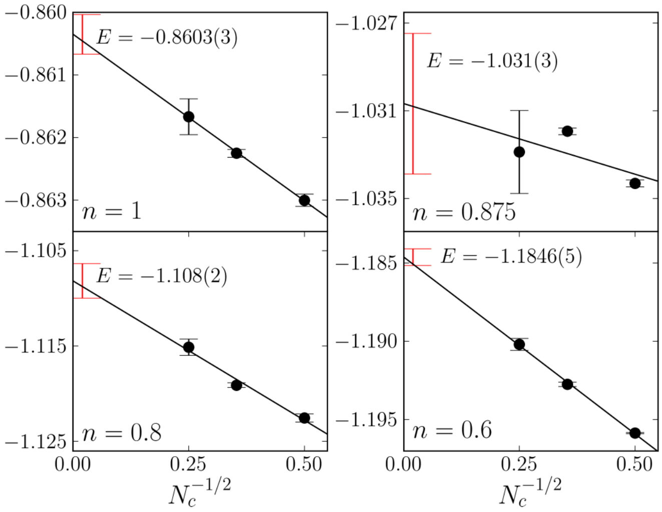

FIG. 10. Cluster size extrapolation for $U = 4, t' = 0$ at various fillings. The black dots are finite size results. The red error bars are the confidence intervals for the thermodynamic limit.

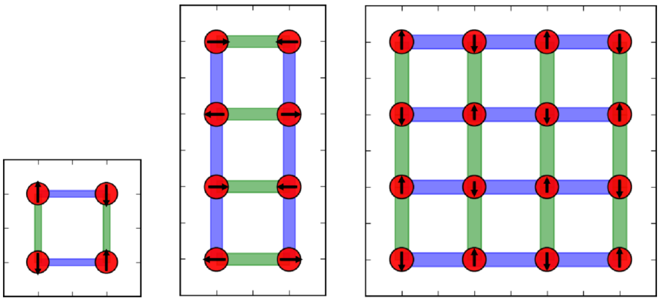

(a)2×2 (b)4×2 (c)4×4

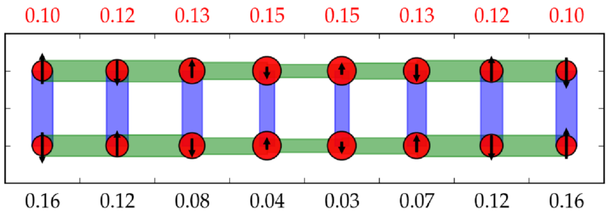

(d)8×2

FIG. 11. Local order parameters for $U = 4, n = 0.875, t' = 0$. The legend is the same as for Fig. 4 in the main text.

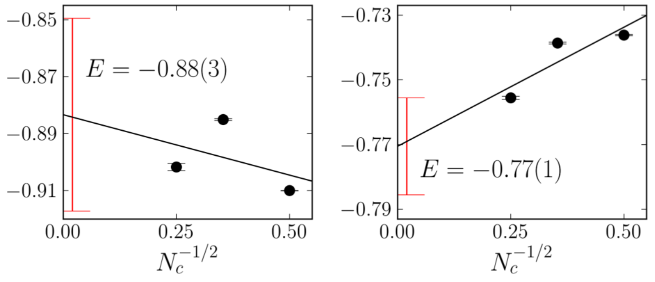

(a)$U = 8$ $n = 0.8$ $t' = 0$ (b)$U = 8$ $n = 0.875$ $t' = -0.2$

FIG. 13. Examples of thermodynamic extrapolations where the energy is sensitive to cluster shape.

For the 4×2 and 8×2 clusters, δ_u appears negligible. For these clusters, we carry out the DMET self-consistency with lower M to obtain the DMET correlation potential u, then do a few final DMRG calculations at large M to extrapolate to the $M \to \infty$ exact solver limit. For 4×4 clusters, the $U = 2$ data are processed in this way as well. However, for other values of U using the 4×4 clusters, the DMRG truncation weight is as large as 10^{-3} for low to intermediate doping with our accessible M, thus making the contribution of δ_u also significant. To compensate for this, we first carry out the DMET self-consistency with a series of different M up to 1200, and linearly extrapolate the energy to the $M = \infty$ limit, E_1. This thus extrapolates errors from *both* sources 1 and 2, assuming $\delta_u \propto \delta_w$. Another further set of DMRG calculations are then done with M up to 2000, using the converged correlation potential from the DMET self-consistency with the largest M. This second set of results is then extrapolated again against the truncated weight to obtain an energy E_2, which only accounts for the error from source 1. Although the linear relation between the source 2 error and the truncation weight need not hold in general, in practice, we find that $\delta_u = \frac{1}{2}|E_1 - E_2|$ gives a crude estimate of δ_u. Therefore, we report the 4×4 cluster energy as $E_{4\times4} = \frac{1}{2}(E_1 + E_2)$, with a final uncertainty of $\delta E_{4\times4}^2 = \delta_u^2 + \delta E_1^2 + \delta E_2^2$, where δE_1 is a combination of the linear regression uncertainty and the uncertainties of the original data points (from DMET self-consistency error), while E_2 does not have any self-consistency error. Figure 9 illustrates the set of computations and linear extrapolations performed with each 4×4 cluster to obtain the 4×4 cluster energy and error estimate.

After obtaining the energy and observables for each cluster size, we extrapolate to the thermodynamic limit using the relation $\Delta E_{N_c} \propto N_c^{-1/2}$. Since both the 4×4 and 2×8 clusters are 16-site clusters, we must choose which one to use

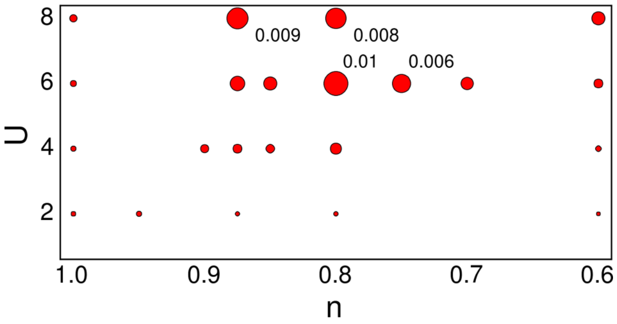

(a)$t' = 0.2$

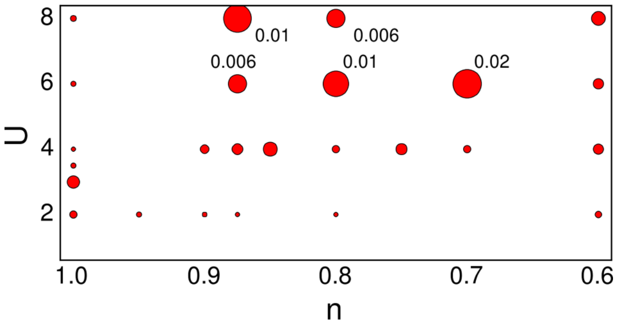

(b)$t' = -0.2$

FIG. 12. DMET energy uncertainty plot for the frustrated Hubbard model with $t' = \pm 0.2$. Refer to Fig. 1(b) in the main text for the legend.

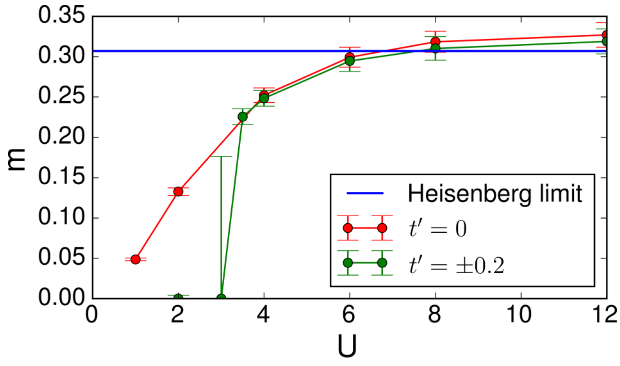

FIG. 14. Staggered magnetization (m) of the half-filled Hubbard model for $t' = \pm 0.2$ and $t' = 0$.

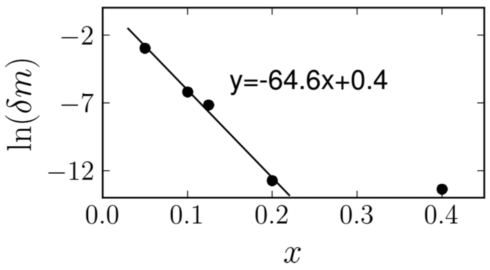

FIG. 15. At $U = 2$, the uncertainty of antiferromagnetic order parameter decreases exponentially with doping. The exponent is 65 ± 4.

in the extrapolation to the thermodynamic limit. We believe that 4×4 clusters have less finite size error than the 8×2 clusters, and thus we generally use these in the extrapolation. However, at certain points in the phase diagram (e.g., at strong coupling, or negative t') there is a strong tendency to inhomogeneity, and the 4×4 clusters cannot necessarily accommodate the new order parameter, resulting in a much higher energy than for the 8×2 cluster. In such cases, namely, when (a) 4×4 and 8×2 clusters show different orders and (b) the 8×2 cluster is lower in energy, we use the 8×2 cluster energy for the extrapolation.

The cluster size extrapolation works surprisingly well given the limited number and small sizes of the clusters, although it contributes the main source of error in the final uncertainty. In Fig. 10 we show some of the extrapolation results at $U = 4$. At half filling and in the overdoped region ($n < 0.8$), the linear relation used in the cluster size extrapolation appears quite good even for these small clusters. In the underdoped region, however, the energy is more strongly dependent on the cluster shape, often because the system has a strong tendency to establish an inhomogeneous phase. In Fig. 11, we plot the local order parameters at $n = 0.875$, where the 8×2 cluster calculation gives an incommensurate antiferromagnetic order. Although the 8×2 cluster energy (-1.0288) is slightly higher than the 4×4 cluster result (-1.033), its inhomogeneity suggests the existence of a low-lying inhomogeneous state that can be (relatively) stabilized by special cluster shapes. Nonetheless, even in the underdoped region, the error model appears to give a reliable estimate of the energy at the thermodynamic limit, albeit with a large uncertainty.

Figure 12 shows the final energy errors for $t' = \pm 0.2$ across the phase diagram. The same plot for $t' = 0$ is shown in Fig. 1(b) in the main text. The overall uncertainty for $t' = 0.2$ is smaller than for $t' = 0$ [see Fig. 1(b) in the main text] and $t' = -0.2$, as is the maximum uncertainty ($0.01t$ compared to $0.03t$ and $0.02t$, respectively). As mentioned before, the main source of error is the cluster size extrapolation. Two examples of large uncertainties due to cluster size (and shape) effect are shown in Fig. 13. The largest uncertainties are observed at $U = 6$ and moderate doping.

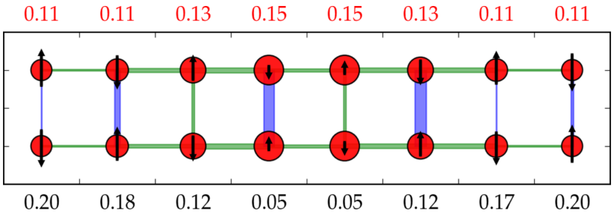

FIG. 16. Inhomogeneous order from 8×2 cluster calculations at $U = 4$, $t' = -0.2$ $n = 0.875$.

TABLE II. Energy comparison for different 16-site impurity clusters at $U = 4$ and $t' = -0.2$.

n	$E_{8\times 2}$	$E_{4\times 4}$
0.8	−1.10483(6)	−1.0507(4)
0.85	−1.0162(1)	−1.020(2)
0.875	−0.9966(1)	−0.9989(7)

APPENDIX C: FURTHER RESULTS

In this section, we expand on the determination of the phase diagram (Fig. 2 in the main text).

The staggered magnetization for the frustrated Hubbard model at half filling (compared to the $t' = 0$ model and the Heisenberg limit) is shown in Fig. 14. Due to particle-hole symmetry, the plot is identical for $t' = \pm 0.2$. The onset of antiferromagnetism is at finite U in the frustrated model, between $U = 2$ and 3.5, consistent with previous QMC simulations [109]. The large error bar at $U = 3$ indicates the sensitivity to impurity cluster sizes near the phase boundary, resulting in a large uncertainty in the thermodynamic extrapolation.

At weak coupling $U = 2$, we find that the antiferromagnetism (in the nonfrustrated model) is destroyed already at

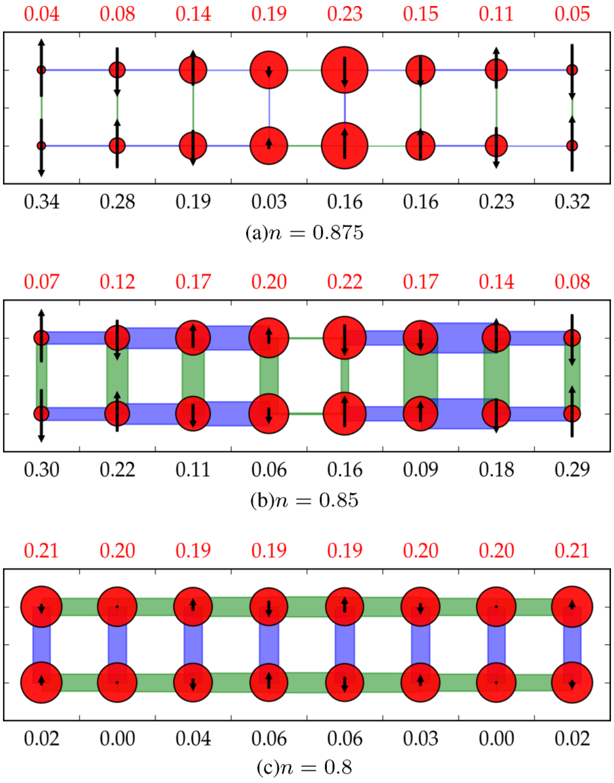

FIG. 17. Inhomogeneous order from 8×2 cluster calculations at $U = 6$ and $t' = 0$ with fillings 0.875 to 0.8.

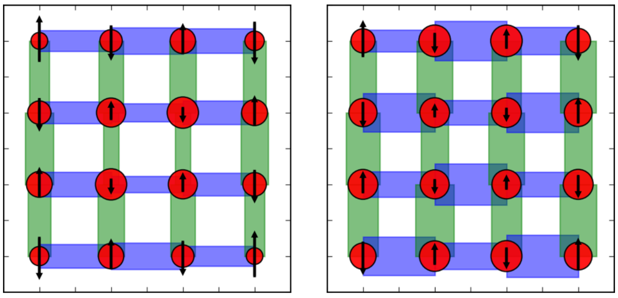

(a)$n = 0.875$ (b)$n = 0.85$

FIG. 18. Local order parameters from 4×4 cluster calculations at $U = 6$ and $t' = 0$ with fillings 0.875 and 0.85.

small doping $x = 0.05$, where the staggered magnetization is $m = 0.00 \pm 0.05$. Although the expectation value is 0, the relatively large uncertainty δm reflects that short-range spin fluctuations are still significant, although long-range order does not exist. As we increase doping, δm decreases exponentially (Fig. 15). At $U = 2$ we do not find d-wave superconductivity to within numerical precision.

We now discuss $U = 4$. We have already shown the order parameters, and the observed thermodynamic extrapolated ground-state orders are all homogeneous. However, for $t' = -0.2$, the 8×2 cluster calculations result in an inhomogeneous state at doping $n = 0.8$–0.875, although the energy is significantly higher than obtained with the 4×4 clusters at the same fillings. An example of inhomogeneous patterns is shown in Fig. 16, where one can see a pair density wave and incommensurate magnetic order. In Table II, we compare the energies between the 8×2 cluster and 4×4 cluster results at relevant points in the phase diagram for $U = 4$. In all these cases, the 8×2 cluster has a higher energy, suggesting that the ground state at $U = 4$ is homogeneous, or inhomogeneous with a very long wavelength that does not fit in our cluster shapes.

At $U = 6$, more interesting inhomogeneous orders start to appear. At $t' = 0$, 8×2 clusters result in various orders (Fig. 17). At both $n = 0.875$ and $n = 0.85$, 4×4 clusters are significantly lower in energy, suggesting the charge, spin, and pairing orders shown in Figs. 17(a) and 17(b) are not stable. At $n = 0.875$, a homogeneous solution with both superconductivity and antiferromagnetism is found [Fig. 18(a)]. However, the thermodynamic extrapolation gives zero for both AF and SC order parameters. At $n = 0.85$, the 4×4 cluster result also shows slight inhomogeneity, with a (π,π) modulation of the d-wave order parameter [Fig. 18(b)]. At $n = 0.8$, where the 8×2 impurity cluster gives a slightly lower

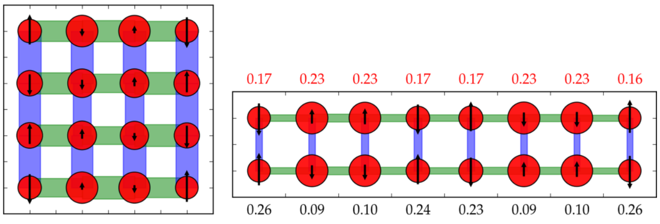

(a) (b)

FIG. 19. Local order parameters for $U = 6$, $n = 0.8$, $t' = -0.2$.

TABLE III. Energy comparison for different 16-site impurity clusters at $U = 8$.

t'	n	$E_{8\times2}$	$E_{4\times4}$
0	0.8	−0.9018(13)	−0.873(6)
0	0.875	−0.7548(4)	−0.748(4)
−0.2	0.8	−0.8487(4)	−0.846(10)
−0.2	0.875	−0.7556(5)	−0.737(7)[a]

[a] The error estimate may not be reliable at this point, because we have only two self-consistent DMET calculations with $M = 1000$ and 1200.

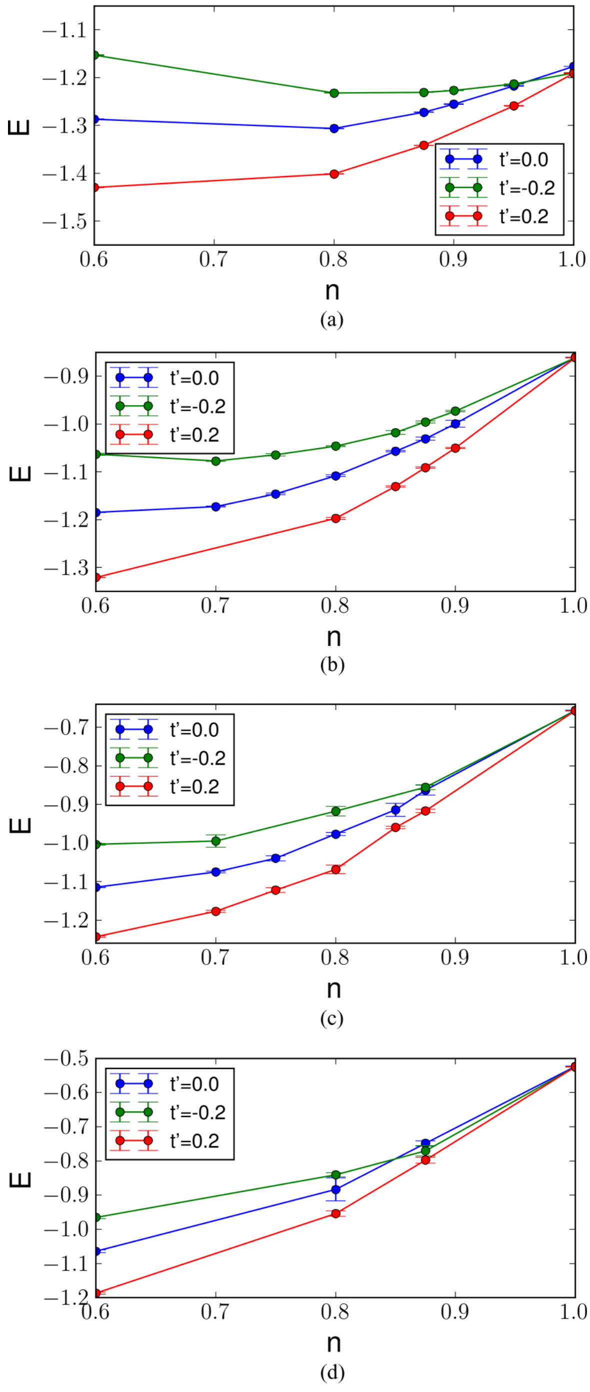

FIG. 20. DMET thermodynamic energy over the phase space: (a) $U = 2$, (b) $U = 4$, (c) $U = 6$, (d) $U = 8$.

energy [$\Delta E = 0.003(2)$], DMET calculations indicate a weak spin density wave [Fig. 17(c)]. This spin density wave may still exist in the thermodynamic limit because the amplitude is comparable to the staggered magnetization in smaller clusters (e.g., $m = 0.04$ for 2×2 clusters).

We now turn to $t' = -0.2$. At $n = 0.8$ and 0.875, 8×2 cluster calculations show inhomogeneous orders. At $n = 0.875$, the pattern is similar to what we observed for $t' = 0$ at the same filling, and its energy $E_{8\times 2} = -0.8402(4)$ is much higher than that of the 4×4 homogeneous solution $E_{4\times 4} = -0.850(3)$. At $n = 0.8$ (Fig. 19), both 4×4 and 8×2 cluster calculations show π-phase shifts in the spin density and d-wave order, while the 8×2 cluster has an additional charge density wave. They are very similar in energy, with $E_{8\times 2} = -0.9283(2)$ and $E_{4\times 4} = -0.927(3)$. This suggests that the ground state here is superconducting with a superimposed spin density wave.

Most results for the underdoped region at $U = 8$ are already shown in the main text (Fig. 4). In Table III, we compare energies for the two 16-site clusters. At all the points shown in the table, the 8×2 cluster gives a lower energy. An unusual result is that at $n = 0.8$, $t' = 0$, the 8×2 cluster shows a *homogeneous* solution, while both the 4×4 and 4×2 clusters give a spin π-phase shift. This unusual behavior, where the 8×2 solution favors homogeneity while the other cluster shapes do not, make thermodynamic extrapolation unreliable and thus gives a large error bar in the thermodynamic estimate of the energy ($\delta E = 0.03$).

Finally, we end our discussion on the results by showing the energies across the phase space in Fig. 20. At half filling, the energy in the frustrated model $t' = \pm 0.2$ is slightly below $t' = 0$, while the difference becomes negligible at large U. At large doping, e.g., $n \leqslant 0.8$, the energy order is dominated by the kinetic effects, i.e., $E_{t'=-0.2} > E_{t'=0} > E_{t'=0.2}$. The energy curves show more complicated behavior in the underdoped region, especially for $t' = 0$ and $t' = -0.2$.

APPENDIX D: DATA SET

In the Supplemental Material [110], we present the energy, chemical potential, and (averaged) order parameters computed and their uncertainties at the thermodynamic limit. Since the averaged order parameters are meaningless when inhomogeneity dominates, we have removed these entries from the table.

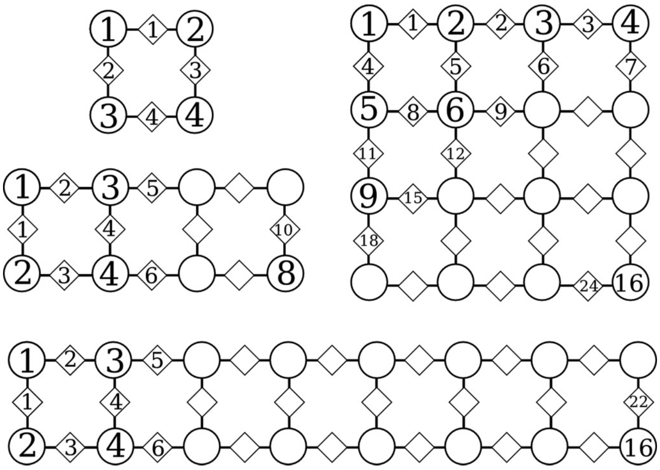

FIG. 21. The encoding of local order parameters for all impurity clusters. Numbers shown in the circles represent the order of sites, which is associated with labeling the charge density and spin density. The numbers in the rhombuses represent the order of bonds, or pairs between neighbor sites, which is associated with labeling the pairing strength. Some numbers are omitted since they are simple to deduce.

In the Supplemental Material [111], we present the results for finite impurity clusters. In addition to the results available at thermodynamic limit, we also present the local order parameters. The local order parameters are encoded in an one-dimensional array, which is explained in figure. The errors shown only include the DMET convergence error, as the other sources of error can be deduced using the procedures described above, from the raw data. We also include the local orders (charge, spin, and pairing strength) in this table as a 1D array. The order of the sites and pairs are shown in Fig. 21.

---

[1] M. C. Gutzwiller, Effect of Correlation on the Ferromagnetism of Transition Metals, Phys. Rev. Lett. **10**, 159 (1963).

[2] J. Kanamori, Electron correlation and ferromagnetism of transition metals, Prog. Theor. Phys. **30**, 275 (1963).

[3] J. Hubbard, Electron correlations in narrow energy bands, in *Proceedings of the Royal Society of London A: Mathematical, Physical and Engineering Sciences* (The Royal Society, London, 1963), Vol. 276, pp. 238–257.

[4] F. C. Zhang and T. M. Rice, Effective Hamiltonian for the superconducting Cu oxides, Phys. Rev. B **37**, 3759 (1988).

[5] E. Dagotto, Correlated electrons in high-temperature superconductors, Rev. Mod. Phys. **66**, 763 (1994).

[6] D. Scalapino, Numerical studies of the 2d Hubbard model, in *Handbook of High-Temperature Superconductivity* (Springer, Berlin, 2007), pp. 495–526.

[7] M. Rigol, T. Bryant, and R. R. P. Singh, Numerical Linked-Cluster Approach to Quantum Lattice Models, Phys. Rev. Lett. **97**, 187202 (2006).

[8] E. Khatami and M. Rigol, Thermodynamics of strongly interacting fermions in two-dimensional optical lattices, Phys. Rev. A **84**, 053611 (2011).

[9] E. Khatami, R. T. Scalettar, and R. R. Singh, Finite-temperature superconducting correlations of the Hubbard model, Phys. Rev. B **91**, 241107(R) (2015).

[10] J. E. Hirsch, Two-dimensional Hubbard model: Numerical simulation study, Phys. Rev. B **31**, 4403 (1985).

[11] A. Georges and G. Kotliar, Hubbard model in infinite dimensions, Phys. Rev. B **45**, 6479 (1992).

[12] A. Georges, G. Kotliar, W. Krauth, and M. J. Rozenberg, Dynamical mean-field theory of strongly correlated fermion

systems and the limit of infinite dimensions, Rev. Mod. Phys. **68**, 13 (1996).
[13] A. N. Rubtsov, M. I. Katsnelson, and A. I. Lichtenstein, Dual fermion approach to nonlocal correlations in the Hubbard model, Phys. Rev. B **77**, 033101 (2008).
[14] G. Rohringer, A. Valli, and A. Toschi, Local electronic correlation at the two-particle level, Phys. Rev. B **86**, 125114 (2012).
[15] H. Schweitzer and G. Czycholl, Weak-coupling treatment of the Hubbard model in one, two and three dimensions, Z. Phys. B: Condens. Matter **83**, 93 (1991).
[16] C. J. Halboth and W. Metzner, Renormalization-group analysis of the two-dimensional Hubbard model, Phys. Rev. B **61**, 7364 (2000).
[17] S. Raghu, S. A. Kivelson, and D. J. Scalapino, Superconductivity in the repulsive Hubbard model: An asymptotically exact weak-coupling solution, Phys. Rev. B **81**, 224505 (2010).
[18] C. N. Varney, C.-R. Lee, Z. J. Bai, S. Chiesa, M. Jarrell, and R. T. Scalettar, Quantum Monte Carlo study of the two-dimensional fermion Hubbard model, Phys. Rev. B **80**, 075116 (2009).
[19] A. C. Cosentini, M. Capone, L. Guidoni, and G. B. Bachelet, Phase separation in the two-dimensional hubbard model: A fixed-node quantum Monte Carlo study, Phys. Rev. B **58**, R14685 (1998).
[20] F. Becca, M. Capone, and S. Sorella, Spatially homogeneous ground state of the two-dimensional Hubbard model, Phys. Rev. B **62**, 12700 (2000).
[21] H. J. M. van Bemmel, D. F. B. ten Haaf, W. van Saarloos, J. M. J. van Leeuwen, and G. An, Fixed-Node Quantum Monte Carlo Method for Lattice Fermions, Phys. Rev. Lett. **72**, 2442 (1994).
[22] L. F. Tocchio, F. Becca, A. Parola, and S. Sorella, Role of backflow correlations for the nonmagnetic phase of the t-t' Hubbard model, Phys. Rev. B **78**, 041101 (2008).
[23] S. Zhang, J. Carlson, and J. E. Gubernatis, Constrained path monte carlo method for fermion ground states, Phys. Rev. B **55**, 7464 (1997).
[24] C.-C. Chang and S. Zhang, Spatially inhomogeneous phase in the two-dimensional repulsive hubbard model, Phys. Rev. B **78**, 165101 (2008).
[25] C.-C. Chang and S. Zhang, Spin and Charge Order in the Doped Hubbard Model: Long-Wavelength Collective Modes, Phys. Rev. Lett. **104**, 116402 (2010).
[26] H. Yokoyama and H. Shiba, Variational Monte-Carlo studies of Hubbard model. i, J. Phys. Soc. Jpn. **56**, 1490 (1987).
[27] D. Eichenberger and D. Baeriswyl, Superconductivity and antiferromagnetism in the two-dimensional Hubbard model: A variational study, Phys. Rev. B **76**, 180504 (2007).
[28] K. Yamaji, T. Yanagisawa, T. Nakanishi, and S. Koike, Variational Monte Carlo study on the superconductivity in the two-dimensional Hubbard model, Physica C: Superconductivity **304**, 225 (1998).
[29] T. Giamarchi and C. Lhuillier, Phase diagrams of the two-dimensional Hubbard and t-J models by a variational Monte Carlo method, Phys. Rev. B **43**, 12943 (1991).
[30] S. R. White and D. J. Scalapino, Phase separation and stripe formation in the two-dimensional t-j model: A comparison of numerical results, Phys. Rev. B **61**, 6320 (2000).
[31] D. J. Scalapino and S. R. White, Numerical results for the Hubbard model: Implications for the high tc pairing mechanism, Found. Phys. **31**, 27 (2001).
[32] S. R. White and D. J. Scalapino, Stripes on a 6-Leg Hubbard Ladder, Phys. Rev. Lett. **91**, 136403 (2003).
[33] M. H. Hettler, A. N. Tahvildar-Zadeh, M. Jarrell, T. Pruschke, and H. R. Krishnamurthy, Nonlocal dynamical correlations of strongly interacting electron systems, Phys. Rev. B **58**, R7475 (1998).
[34] M. H. Hettler, M. Mukherjee, M. Jarrell, and H. R. Krishnamurthy, Dynamical cluster approximation: Nonlocal dynamics of correlated electron systems, Phys. Rev. B **61**, 12739 (2000).
[35] A. I. Lichtenstein and M. I. Katsnelson, Antiferromagnetism and d-wave superconductivity in cuprates: A cluster dynamical mean-field theory, Phys. Rev. B **62**, R9283 (2000).
[36] G. Kotliar, S. Y. Savrasov, G. Pálsson, and G. Biroli, Cellular Dynamical Mean Field Approach to Strongly Correlated Systems, Phys. Rev. Lett. **87**, 186401 (2001).
[37] M. Potthoff, M. Aichhorn, and C. Dahnken, Variational Cluster Approach to Correlated Electron Systems in Low Dimensions, Phys. Rev. Lett. **91**, 206402 (2003).
[38] C. Dahnken, M. Aichhorn, W. Hanke, E. Arrigoni, and M. Potthoff, Variational cluster approach to spontaneous symmetry breaking: The itinerant antiferromagnet in two dimensions, Phys. Rev. B **70**, 245110 (2004).
[39] M. Aichhorn and E. Arrigoni, Weak phase separation and the pseudogap in the electron-doped cuprates, Europhys. Lett. **72**, 117 (2005).
[40] D. Sénéchal, P.-L. Lavertu, M.-A. Marois, and A.-M. S. Tremblay, Competition Between Antiferromagnetism and Superconductivity in High-T_c Cuprates, Phys. Rev. Lett. **94**, 156404 (2005).
[41] M. Aichhorn, E. Arrigoni, M. Potthoff, and W. Hanke, Antiferromagnetic to superconducting phase transition in the hole- and electron-doped Hubbard model at zero temperature, Phys. Rev. B **74**, 024508 (2006).
[42] C. J. Halboth and W. Metzner, d-Wave Superconductivity and Pomeranchuk Instability in the Two-Dimensional Hubbard Model, Phys. Rev. Lett. **85**, 5162 (2000).
[43] H. J. Schulz, Incommensurate Antiferromagnetism in the Two-Dimensional Hubbard Model, Phys. Rev. Lett. **64**, 1445 (1990).
[44] S. R. White, D. J. Scalapino, R. L. Sugar, E. Y. Loh, J. E. Gubernatis, and R. T. Scalettar, Numerical study of the two-dimensional Hubbard model, Phys. Rev. B **40**, 506 (1989).
[45] A. V. Chubukov and K. A. Musaelian, Magnetic phases of the two-dimensional Hubbard model at low doping, Phys. Rev. B **51**, 12605 (1995).
[46] P. A. Igoshev, M. A. Timirgazin, A. A. Katanin, A. K. Arzhnikov, and V. Y. Irkhin, Incommensurate magnetic order and phase separation in the two-dimensional Hubbard model with nearest- and next-nearest-neighbor hopping, Phys. Rev. B **81**, 094407 (2010).
[47] M. Capone and G. Kotliar, Competition between d-wave superconductivity and antiferromagnetism in the two-dimensional Hubbard model, Phys. Rev. B **74**, 054513 (2006).
[48] E. Gull, O. Parcollet, and A. J. Millis, Superconductivity and the Pseudogap in the Two-Dimensional Hubbard Model, Phys. Rev. Lett. **110**, 216405 (2013).

[49] M. Kato, K. Machida, H. Nakanishi, and M. Fujita, Soliton lattice modulation of incommensurate spin density wave in two dimensional Hubbard model -a mean field study-, J. Phys. Soc. Jpn. **59**, 1047 (1990).

[50] A. Moreo, D. J. Scalapino, R. L. Sugar, S. R. White, and N. E. Bickers, Numerical study of the two-dimensional Hubbard model for various band fillings, Phys. Rev. B **41**, 2313 (1990).

[51] M. Miyazaki, K. Yamaji, and T. Yanagisawa, Possible coexistence of superconductivity and static sdw stripes in the two-dimensional Hhubbard model, J. Phys. Chem. Solids **63**, 1403 (2002).

[52] T. Mizusaki and M. Imada, Gapless quantum spin liquid, stripe, and antiferromagnetic phases in frustrated Hubbard models in two dimensions, Phys. Rev. B **74**, 014421 (2006).

[53] T. A. Maier, M. Jarrell, and D. J. Scalapino, Pairing interaction in the two-dimensional Hubbard model studied with a dynamic cluster quantum Monte Carlo approximation, Phys. Rev. B **74**, 094513 (2006).

[54] T. A. Maier, M. Jarrell, T. C. Schulthess, P. R. C. Kent, and J. B. White, Systematic Study of d-Wave Superconductivity in the 2d Repulsive Hubbard Model, Phys. Rev. Lett. **95**, 237001 (2005).

[55] A. Macridin, M. Jarrell, and T. Maier, Absence of the d-density-wave state from the two-dimensional Hubbard model, Phys. Rev. B **70**, 113105 (2004).

[56] M. Jarrell, T. Maier, M. H. Hettler, and A. N. Tahvildarzadeh, Phase diagram of the Hubbard model: Beyond the dynamical mean field, Europhys. Lett. **56**, 563 (2001).

[57] J. Otsuki, H. Hafermann, and A. I. Lichtenstein, Superconductivity, antiferromagnetism, and phase separation in the two-dimensional Hubbard model: A dual-fermion approach, Phys. Rev. B **90**, 235132 (2014).

[58] K.-S. Chen, Z. Y. Meng, T. Pruschke, J. Moreno, and M. Jarrell, Lifshitz transition in the two-dimensional Hubbard model, Phys. Rev. B **86**, 165136 (2012).

[59] G. Knizia and G. K.-L. Chan, Density Matrix Embedding: A Simple Alternative to Dynamical Mean-Field Theory, Phys. Rev. Lett. **109**, 186404 (2012).

[60] G. Knizia and G. K.-L. Chan, Density matrix embedding: A strong-coupling quantum embedding theory, J. Chem. Theory Comput. **9**, 1428 (2013).

[61] Q. Chen, G. H. Booth, S. Sharma, G. Knizia, and G. K.-L. Chan, Intermediate and Spin-Liquid Phase of the Half-Filled Honeycomb Hubbard Model, Phys. Rev. B **89**, 165134 (2014).

[62] I. W. Bulik, G. E. Scuseria, and J. Dukelsky, Density matrix embedding from broken symmetry lattice mean fields, Phys. Rev. B **89**, 035140 (2014).

[63] Z. Fan and Q.-l. Jie, Cluster density matrix embedding theory for quantum spin systems, Phys. Rev. B **91**, 195118 (2015).

[64] Q. Sun and G. K.-L. Chan, Exact and optimal quantum mechanics/molecular mechanics boundaries, J. Chem. Theory Comput. **10**, 3784 (2014).

[65] I. W. Bulik, W. Chen, and G. E. Scuseria, Electron correlation in solids via density embedding theory, J. Chem. Phys. **141**, 054113 (2014).

[66] G. H. Booth and G. K.-L. Chan, Spectral functions of strongly correlated extended systems via an exact quantum embedding, Phys. Rev. B **91**, 155107 (2015).

[67] I. Peschel, Special review: Entanglement in solvable many-particle models, Braz. J. Phys. **42**, 267 (2012).

[68] G. K.-L. Chan and S. Sharma, The density matrix renormalization group in quantum chemistry, Annu. Rev. Phys. Chem. **62**, 465 (2011).

[69] S. R. White and A. L. Chernyshev, Neel Order in Square and Triangular Lattice Heisenberg Models, Phys. Rev. Lett. **99**, 127004 (2007).

[70] T. A. Maier and M. Jarrell, Comparison of two-quantum-cluster approximations, Phys. Rev. B **65**, 041104 (2002).

[71] M. Qin and S. Zhang (private communication).

[72] S. Zhang and H. Krakauer, Quantum Monte Carlo Method Using Phase-Free Random Walks with Slater Determinants, Phys. Rev. Lett. **90**, 136401 (2003).

[73] S. White (private communication).

[74] J. P. F. LeBlanc and E. Gull, Equation of state of the fermionic two-dimensional Hubbard model, Phys. Rev. B **88**, 155108 (2013).

[75] M. Aichhorn, E. Arrigoni, M. Potthoff, and W. Hanke, Phase separation and competition of superconductivity and magnetism in the two-dimensional Hubbard model: From strong to weak coupling, Phys. Rev. B **76**, 224509 (2007).

[76] A. W. Sandvik, Finite-size scaling of the ground-state parameters of the two-dimensional Heisenberg model, Phys. Rev. B **56**, 11678 (1997).

[77] W. Metzner and D. Vollhardt, Ground-state energy of the d=1,2,3 dimensional Hubbard model in the weak-coupling limit, Phys. Rev. B **39**, 4462 (1989).

[78] E. Pavarini, I. Dasgupta, T. Saha-Dasgupta, O. Jepsen, and O. K. Andersen, Band-Structure Trend in Hole-Doped Cuprates and Correlation with t_{cmax}, Phys. Rev. Lett. **87**, 047003 (2001).

[79] Z. B. Huang, H. Q. Lin, and J. E. Gubernatis, Quantum Monte Carlo study of spin, charge, and pairing correlations in the $t - t^{'} - u$ Hubbard model, Phys. Rev. B **64**, 205101 (2001).

[80] A. Eberlein and W. Metzner, Superconductivity in the two-dimensional t-$t^{'}$-Hubbard model, Phys. Rev. B **89**, 035126 (2014).

[81] S. Zhang, J. Carlson, and J. E. Gubernatis, Pairing Correlations in the Two-Dimensional Hubbard Model, Phys. Rev. Lett. **78**, 4486 (1997).

[82] J. P. F. LeBlanc, A. E. Antipov, F. Becca, I. W. Bulik, G. K.-L. Chan, C.-M. Chung, Y. Deng, M. Ferrero, T. M. Henderson, C. A. Jiménez-Hoyos *et al.*, Solutions of the Two Dimensional Hubbard Model: Benchmarks and Results from a Wide Range of Numerical Algorithms, Phys. Rev. X **5**, 041041 (2015).

[83] D. J. Scalapino, E. Loh, and J. E. Hirsch, d-wave pairing near a spin-density-wave instability, Phys. Rev. B **34**, 8190 (1986).

[84] R. Peters and N. Kawakami, Spin density waves in the Hubbard model: A DMFT approach, Phys. Rev. B **89**, 155134 (2014).

[85] A. Leprévost, O. Juillet, and R. Frésard, Intertwined orders from symmetry projected wavefunctions of repulsively interacting Fermi gases in optical lattices, New J. Phys. **17**, 103023 (2015).

[86] D. Poilblanc and T. M. Rice, Charged solitons in the Hartree-Fock approximation to the large-U Hubbard model, Phys. Rev. B **39**, 9749 (1989).

[87] M. Vojta and S. Sachdev, Charge Order, Superconductivity, and a Global Phase Diagram of Doped Antiferromagnets, Phys. Rev. Lett. **83**, 3916 (1999).

[88] A. Melikyan and Z. Tešanović, Model of phase fluctuations in a lattice d-wave superconductor: Application to the Cooper-pair charge-density wave in underdoped cuprates, Phys. Rev. B **71**, 214511 (2005).

[89] H.-D. Chen, O. Vafek, A. Yazdani, and S.-C. Zhang, Pair Density Wave in the Pseudogap State of High Temperature Superconductors, Phys. Rev. Lett. **93**, 187002 (2004).

[90] P. A. Lee, Amperean pairing and the pseudogap phase of cuprate superconductors, Phys. Rev. X **4**, 031017 (2014).

[91] E. Berg, E. Fradkin, and S. A. Kivelson, Charge-4e superconductivity from pair-density-wave order in certain high-temperature superconductors, Nat. Phys. **5**, 830 (2009).

[92] S. R. White and D. J. Scalapino, Density Matrix Renormalization Group Study of the Striped Phase in the 2d t-j Model, Phys. Rev. Lett. **80**, 1272 (1998).

[93] C. S. Hellberg and E. Manousakis, Stripes and the t-J Model, Phys. Rev. Lett. **83**, 132 (1999).

[94] G. Hager, G. Wellein, E. Jeckelmann, and H. Fehske, Stripe formation in doped Hubbard ladders, Phys. Rev. B **71**, 075108 (2005).

[95] P. Corboz, S. R. White, G. Vidal, and M. Troyer, Stripes in the two-dimensional t-j model with infinite projected entangled-pair states, Phys. Rev. B **84**, 041108 (2011).

[96] V. V. Moshchalkov, J. Vanacken, and L. Trappeniers, Phase diagram of high-T_c cuprates: Stripes, pseudogap, and effective dimensionality, Phys. Rev. B **64**, 214504 (2001).

[97] M. Fleck, A. I. Lichtenstein, and A. M. Oleś, Spectral properties and pseudogap in the stripe phases of cuprate superconductors, Phys. Rev. B **64**, 134528 (2001).

[98] T. Valla, A. Fedorov, J. Lee, J. Davis, and G. Gu, The ground state of the pseudogap in cuprate superconductors, Science **314**, 1914 (2006).

[99] J.-X. Li, C.-Q. Wu, and D.-H. Lee, Checkerboard charge density wave and pseudogap of high-T_c cuprate, Phys. Rev. B **74**, 184515 (2006).

[100] T. A. Sedrakyan and A. V. Chubukov, Pseudogap in underdoped cuprates and spin-density-wave fluctuations, Phys. Rev. B **81**, 174536 (2010).

[101] P. Corboz, Improved energy extrapolation with infinite projected entangled-pair states applied to the 2d Hubbard model, arXiv:1508.04003.

[102] P.-G. de Gennes, *Superconductivity of Metals and Alloys* (Benjamin, New York, 1966).

[103] D. Yamaki, T. Ohsaku, H. Nagao, and K. Yamaguchi, Formulation of unrestricted and restricted Hartree-Fock-Bogoliubov equations, Int. J. Quantum Chem. **96**, 10 (2004).

[104] J. Bardeen, L. N. Cooper, and J. R. Schrieffer, Theory of superconductivity, Phys. Rev. **108**, 1175 (1957).

[105] S. Datta and P. F. Bagwell, Can the Bogoliubov-de Gennes equation be interpreted as a 'one-particle' wave equation?, Superlattices Microstruct. **25**, 1233 (1999).

[106] G. K.-L. Chan and M. Head-Gordon, Highly correlated calculations with a polynomial cost algorithm: A study of the density matrix renormalization group, J. Chem. Phys. **116**, 4462 (2002).

[107] G. K.-L. Chan, An algorithm for large scale density matrix renormalization group calculations, J. Chem. Phys. **120**, 3172 (2004).

[108] S. Sharma and G. K.-L. Chan, Spin-adapted density matrix renormalization group algorithms for quantum chemistry, J. Chem. Phys. **136**, 124121 (2012).

[109] H. Q. Lin and J. E. Hirsch, Two-dimensional Hubbard model with nearest- and next-nearest-neighbor hopping, Phys. Rev. B **35**, 3359 (1987).

[110] Please see Supplemental Material at http://link.aps.org/supplemental/10.1103/PhysRevB.93.035126 for the energy, chemical potential, and (averaged) order parameters and their uncertainties at the thermodynamic limit.

[111] Please see Supplemental Material at http://link.aps.org/supplemental/10.1103/PhysRevB.93.035126 for the energy, chemical potential and (local and averaged) order parameters of finite impurity clusters.